A&A 515, A8 (2010)
DOI: 10.1051/0004-6361/200912058

Astronomy & Astrophysics

Mid- and far-infrared luminosity functions and galaxy evolution from multiwavelength *Spitzer* observations up to $z \sim 2.5$

G. Rodighiero[1], M. Vaccari[1], A. Franceschini[1], L. Tresse[2], O. Le Fevre[2], V. Le Brun[2], C. Mancini[3,4,5], I. Matute[3,6], A. Cimatti[5], L. Marchetti[1], O. Ilbert[2,7], S. Arnouts[2,8], M. Bolzonella[9], E. Zucca[9], S. Bardelli[9], C. J. Lonsdale[10], D. Shupe[10], J. Surace[10], M. Rowan-Robinson[11], B. Garilli[12], G. Zamorani[9], L. Pozzetti[9], M. Bondi[13], S. de la Torre[2], D. Vergani[9], P. Santini[14,15], A. Grazian[15], and A . Fontana[15]

[1] Department of Astronomy, University of Padova, Vicolo dell'Osservatorio 3, 35122 Padova, Italy
e-mail: giulia.rodighiero@unipd.it
[2] Laboratoire d'Astrophysique de Marseille, OAMP, UMR6110, CNRS-Université de Provence, 38 rue Frederic Joliot-Curie, 13388 Cedex 13, France
[3] Dipartimento di Astronomia e Scienza dello Spazio, Università degli Studi di Firenze, Largo E. Fermi 3 50125, Firenze, Italy
[4] Osservatorio Astrofisico di Arcetri (OAF), INAF-Firenze, Largo E. Fermi 5, 50125 Firenze, Italy
[5] Dipartimento di Astronomia, Università di Bologna, via Ranzani 1, 40127 Bologna, Italy
[6] Dipartimento di Fisica E. Amaldi, Università degli Studi Roma Tre, via della Vasca 84, 00146 Roma, Italy
[7] Institute for Astronomy, 2680 Woodlawn Dr., University of Hawaii, Honolulu, Hawaii, 96822, USA
[8] Canada France Hawaii Telescope corporation, Mamalahoa Hwy, Kamuela, 96743, USA
[9] INAF-Osservatorio Astronomico di Bologna, via Ranzani 1, 40127, Bologna, Italy
[10] Infrared Processing and Analysis Center, California Institute of Technology, 100-22, Pasadena, CA 91125, USA
[11] Astrophysics Group, Blackett Laboratory, Imperial College of Science Technology and Medicine, Prince Consort Road, London SW7 2BZ, UK
[12] IASF-INAF, Via Bassini 15, 20133, Milano, Italy
[13] IRA-INAF, Via Gobetti 101, 40129, Bologna, Italy
[14] Dipartimento di Fisica, Università di Roma La Sapienza, P.le A. Moro 2, 00185 Roma, Italy
[15] INAF - Osservatorio Astronomico di Roma, via Frascati 33, 00040 Monteporzio (RM), Italy

Received 13 March 2009 / Accepted 21 November 2009

ABSTRACT

Context. Studies of the infrared (IR) emission of cosmic sources have proven essential to constraining the evolutionary history of cosmic star formation and the gravitational accretion of nuclear black holes, because many of these events occur inside heavily dust-extinguished environments.

Aims. The *Spitzer Space Telescope* has provided a large amount of data to constrain the nature and cosmological evolution of infrared source populations. In the present paper we exploit a large homogeneous dataset to derive a self-consistent picture of IR emission based on the time-dependent $\lambda_{\rm eff}$ = 24, 15, 12, and 8 μm monochromatic and bolometric IR luminosity functions (LF) over the full $0 < z < 2.5$ redshift range.

Methods. Our present analysis is based on a combination of data from deep *Spitzer* surveys of the VIMOS VLT Deep Survey (VVDS-SWIRE) and GOODS fields. To our limiting flux of $S_{24} = 400$ μJy, our sample derived from VVDS-SWIRE includes 1494 sources, and 666 and 904 sources brighter than $S_{24} = 80$ μJy are catalogued in GOODS-S and GOODS-N, respectively, for a total area of ~0.9 square degrees. Apart from a few galaxies, we obtain reliable optical identifications and redshifts for all these sources, providing a rich and robust dataset for our luminosity function determination. The final combined reliable sample includes 3029 sources, the fraction with photometric redshifts being 72% over all redshifts and almost all galaxies at $z > 1.5$. Based on the multiwavelength information available in these areas, we constrain the LFs at 8, 12, 15, and 24 μm. We also infer the total IR luminosities from our best-fit model of the observed SEDs of each source, and use this to derive the bolometric (8−1000 μm) LF and comoving volume emissivity to $z \sim 2.5$.

Results. In the redshift interval $0 < z < 1$, the bolometric IR luminosity density evolves as $(1+z)^{3.8\pm0.4}$. Although it is more uncertain at higher-z, our results show a flattening in the IR luminosity density at $z > 1$. The mean redshift of the peak in the source number density shifts with luminosity: the brightest IR galaxies appear to form stars at earlier cosmic times ($z > 1.5$), while star formation in the less luminous galaxies continues until more recent epochs ($z \sim 1$ for $L_{\rm IR} < 10^{11}$ $L_{\odot}$), in overall agreement with similar analyses in the literature.

Conclusions. Our results are indicative of a rapid increase in the galaxy IR comoving volume emissivity up to $z \sim 1$ and a constant average emissivity at $z > 1$. We also appear to measure a difference in the evolutionary rate of the source number densities as a function of luminosity, which is consistent with the *downsizing* evolutionary patterns reported for other samples of cosmic sources.

Key words. galaxies: evolution – galaxies: fundamental parameters – galaxies: luminosity function, mass function – infrared: galaxies – cosmology: observations – surveys

1. Introduction

A remarkable property of infrared (IR) selected extragalactic sources is their rapid evolutionary rates with redshift, which exceed those measured for galaxies at any other wavelength. Based on data acquired by the *Infrared Astronomical Satellite* (*IRAS*), strong evolution was detected within the narrow $0 < z < 0.2$ redshift range at far-IR wavelengths (60 μm) by Hacking et al. (1987), Franceschini et al. (1988), and Saunders et al. (1990). The IRAS all-sky coverage also inspired Fang et al. (1998) and Shupe et al. (1998) to establish local benchmarks at mid-IR wavelengths (12 and 25 μm). The *Infrared Space Observatory* (*ISO*) enabled the first deep surveys of distant IR sources to be performed in the mid- and far-IR, to $z \sim 1$ (Elbaz et al. 1999; Puget et al. 1999). These surveys found that dust-enshrouded starbursts undergo strong evolution in both luminosity and density up to this redshift (e.g., Franceschini et al. 2001; Chary & Elbaz 2001; Elbaz et al. 2002; Pozzi et al. 2004).

The ISO results have been extended in redshift to $z > 1$ by the *Spitzer Space Telescope* (Papovich et al. 2004; Marleau et al. 2004; Dole et al. 2004; Lagache et al. 2004), which has improved sensitivity and spatial resolution between 3.6 and 160 μm compared to previous IR observatories. In particular, Le Floc'h et al. (2005) studied the evolution of IR-bright sources to $z \sim 1$ using a sample of mid-infrared (24 μm) sources with complete redshift information and deriving their rest-frame 15 μm and total IR LFs. Significant evolution of the IR-selected population with lookback time in both luminosity and density was found in agreement with previous results. Similarly, Perez-Gonzalez et al. (2005) fitted the rest-frame 12 μm LFs in various redshift bins across the range $0 < z < 3$, based on photometric redshift determinations, therefore constraining the evolution of IR-bright star-forming galaxies. Caputi et al. (2007) present the rest-frame 8 μm LF of star-forming galaxies in two bins at $z \sim 1$ and $z \sim 2$. Based on an early reduction of SWIRE EN1 field data and using photometric redshifts based on relatively shallow optical imaging, Babbedge et al. (2006) computed the mid-IR (8 and 24 μm) galaxy (AGN1) LF to $z \sim 2$ ($z \sim 4$; albeit with uncertainties that strongly increase with redshift). *Spitzer* (Werner et al. 2004) studies have also allowed accurate determinations of the *local* (or low-redshift) LFs at 8 and 24 μm (Huang et al. 2007; and Marleau et al. 2007; Vaccari et al. 2009, in preparation), which provide important data sets for comparison with high-z sources.

All of these studies detect significant evolution in the IR population up to $z \sim 1$, including a comoving luminosity density, produced by luminous IR galaxies, that is more than 10 times higher at $z \sim 1$ than in the local Universe. This evolution levels off at higher redshift, up to the highest currently probed by *Spitzer*, $z \sim 3$. Moreover, luminous and ultra-luminous IR sources, i.e. LIRGs and ULIRGs, are the predominant contributors to the comoving infrared energy density above $z \sim 0.5$ and represent 70% of the star-forming activity at $z \sim 1$ (Le Floc'h et al. 2005).

To improve our knowledge of the evolutionary properties of *Spitzer*-selected sources, we analyze a combination of data from the GOODS and VVDS-SWIRE multiwavelength surveys to determine mid-IR and bolometric luminosity functions (and thus estimate the SFR density) over a wide redshift interval, $0 < z < 2.5$. By combining data from three distinct areas of sky, we are able to strongly reduce the effects cosmic variance. The coverage of the luminosity-redshift plane is also improved by combining of surveys with two limiting fluxes, the deeper GOODS surveys (80 μJy limit) and the shallower wider-area VVDS-SWIRE (400 μJy limit) survey, which have similar numbers of sources in the two flux regimes. The redshift information was optimized by including a large number of new spectroscopic redshifts from public databases in the GOODS fields and a highly sophisticated photometric redshift analysis in the wide-area VVDS-SWIRE field, taking advantage of the deep multiwavelength photometry available and VVDS-based photometric redshift tools. Because we have more than 3000 objects in our combined sample, we are able to consider many narrow redshift bins in the LF determination. The extremely rich suite of complementary data from the UV to the far-IR available in the three fields also allows us to perform a robust characterization of source spectra, computing reliable K-corrections and determining spectral extrapolations to apply to our LF determination.

At the same time, the large amount of multi-band photometric data available for all our sample sources allows us to compute reliable bolometric corrections for the rest-frame 24 μm and the total (8−1000 μm) luminosities. These correction factors are particularly well established because the 24 μm flux is an excellent *proxy* for the bolometric flux of active galaxies at high redshift (for high-z sources, longer wavelength fluxes are usually not available), see e.g., Caputi et al. (2007), Bavouzet et al. (2008). For these reasons, we believe that our constraints on the evolutionary comoving luminosity density and star-formation rate that we discuss in the paper are among the most robust determined to date.

The paper is structured as follows. In Sect. 2, we introduce the VVDS-SWIRE 24 μm dataset, which was first employed here. In Sect. 3, we describe the multiwavelength identification and redshift determination process for 24 μm sources in the GOODS and SWIRE fields. In Sect. 5 we explain the procedure adopted to derive the monochromatic mid-IR rest-frame luminosities. Section 5 is devoted to describing the computation of the LFs with the $1/V_{\rm max}$ technique and comparing our results with previously published data for various IR bands. The bolometric LF is also presented. Finally, in Sect. 6 we discuss our results for the evolution of the bolometric LF and the IR luminosity density with redshift, and compare our results with model predictions. A summary of or paper is presented in Sect. 7.

We adopt throughout a cosmology with $H_0 = 70\ {\rm km\,s^{-1}\,Mpc^{-1}}$, $\Omega_{\rm M} = 0.3$, and $\Omega_\Lambda = 0.7$. We indicate with the symbol L_{24} the luminosity at 24 μm in erg/s (νL_ν, and similarly for other wavelengths).

2. Spitzer observations of the VVDS-SWIRE field

The 02 hour field portion of the VIMOS VLT Deep Survey (VVDS, Le Févre et al. 2004a,b and 2005) is located within the XMM-LSS area of the *Spitzer* Wide-area InfraRed Extragalactic survey (SWIRE, Lonsdale et al. 2003, 2006). The total area jointly covered by the two surveys on the sky (hereafter, the VVDS-SWIRE area) is ∼0.85 square degrees.

The *Spitzer* observations of the six SWIRE fields were carried out between December 2003 and December 2004. The 24 μm observations were executed using the MIPS Scan Map AOT with a medium scan rate. Two passes separated by half a field-of-view were carried out to ensure the accurate removal of cosmic rays and transient sources (e.g., asteroids), providing a total exposure time of at least 160 s per pointing, while overlaps between rotated scans provided deeper coverage in some portions of each map.

The raw data were reduced using the *Spitzer Science Center* (SSC) standard pipeline. The data processing started from the basic calibrated data (BCD) and median filtering was employed to reduce variations in the local background. While this filtering

optimizes faint source detection, it might also cause some loss of information about the extended background level in the field. However, this only affects extended or bright ($S_{24} > 0.2$ Jy) sources, and is thus not an issue for our sample, which consists mostly of point-like faint sources. A slightly more sophisticated scheme than those applied to other SWIRE fields had to be put in place to remove latent artifacts in the XMM-LSS field caused by the proximity of the bright Mira star. Corrected BCDs were coadded into large mosaics using the SSC's MOPEX package. Source extraction and photometry is described in Sect. 3.1.

Shupe et al. (2008) have presented the analysis of 24 μm source counts in the SWIRE fields, which have a (differential) completeness of 75% at $S(24\ \mu\mathrm{m}) = 400\ \mu$Jy. In the present work, however, we employed a yet deeper source catalog produced as part of the SWIRE final catalog (Surace et al., in prep). This catalog is based on the same SWIRE dataset used by Shupe et al. (2008) but extracts sources using APEX (a software tool provided by SSC) rather than SExtractor (formerly used by Shupe et al. 2008) to a lower signal-to-noise ratio (SNR). We adopted APEX default flux measurements based on PRF fitting, as recommended by SSC and described in the MIPS Data Handbook (SSC, 2007, Version 3.3.1), and calibrated measured fluxes based on Engelbracht et al. (2007). Following the MIPS Data Handbook, we then multiplied the APEX fluxes by 1.15 to complete an aperture correction, i.e., take into account the fraction of the PSF scattered to large radii, and then divided them by 0.961 to perform a color correction that is appropriate for an SED with a constant νS_ν. The differential completeness of this deeper catalog is estimated to be superior to 90% at $S(24\ \mu\mathrm{m}) = 400\ \mu$Jy in the XMM-LSS area, while its reliability at this lower SNR is ensured by the presence of a close optical and IRAC counterpart (see Sect. 3.1). We therefore adopted this relatively shallow, but highly reliable, 24 μm flux limit in the VVDS-SWIRE region, as a wide-area complement to the deeper GOODS datasets described in the following section. Our 24 μm reference catalog contains 1494 sources with $S(24\ \mu\mathrm{m}) > 400\ \mu$Jy.

3. Multiwavelength identification and analysis of the Spitzer MIPS 24 μm sources

Our derivation of MIR and bolometric luminosity functions in the present paper is based on a *Spitzer* MIPS 24 μm sample selection. We now describe the complex procedures involved in the source identification for our three reference fields, the VVDS/SWIRE, and GOODS-S and GOODS-N fields, covering a total area of ∼0.9 square degrees.

3.1. VVDS-SWIRE

We derived an observational SED for each 24 μm source detected in the VVDS-SWIRE region by exploiting the rich multiwavelength information available from the VVDS database[1]. These data include accurate photometry in the optical/NIR spectral range (see descriptions in Arnouts et al. 2007; and de la Torre et al. 2007), including deep multicolor photometry ($u^*g'r'i'z'$) from the Canada-France-Hawaii Telescope Legacy Survey (CFHTLS-D1) and the VIMOS VLT Deep Survey (VVDS), consisting of deep photometry (Le Fevre et al. 2005) in the B, V, R, I, J, K bands and VIMOS spectroscopy. Both J and K data are also available from the UKIDSS Ultra Deep Survey (Lawrence et al. 2007) based on the DR1 release (Warren et al. 2007). The SWIRE IRAC photometry is based on the band-merged catalog that includes 3.6, 4.5, 5.8, and 8.0 μm passband data (Surace et al. 2005), with a typical 5σ depth of 5.0, 9.0, 43, and 40 μJy respectively. As in Arnouts et al. (2007), we used the flux measurements derived in 3 arcsec apertures for faint sources, while we adopted adaptive apertures (as for Kron magnitudes in Bertin & Arnouts 1996) for bright sources ($m_{\mathrm{AB}}(3.6) < 19.5$).

Photometric redshifts computed by Arnouts et al. (2007) are also available in the VVDS database (see also McCracken et al. 2003; Radovich et al. 2004; Iovino et al. 2005). These were estimated using the χ^2 fitting algorithm Le Phare[2] and calibrated with the VVDS first epoch spectroscopic redshifts (providing ∼1500 secure spectra for sources with $m_{\mathrm{AB}}(3.6\ \mu\mathrm{m}) < 21.5$) in the same dataset as described in Ilbert et al. (2006), which includes the 3.6 μm and 4.5 μm infrared photometry from SWIRE (Lonsdale et al. 2003). The accuracy achieved in the photometric redshift determination is $\sigma[\Delta z/(1+z)] \sim 0.031$ with no systematic shift. The photometric redshifts have values in the range $0 < z < 2$ (the high-z tail at $z > 1.4$ being unable to be verified with spectroscopic data at that time (Arnouts et al. 2007).

The cross-correlation of the SWIRE 24 μm catalog with the VVDS multiwavelength database was carried out using a nearest-neighbor association with a 2 arcsec search radius, since at these bright flux levels ($S[24\ \mu\mathrm{m}] > 400\ \mu$Jy) confusion is not a major issue as in the GOODS case. The entire sample of 1494 sources detected at 24 μm over the VVDS-SWIRE region was thus assigned an optical/NIR counterpart. For 69 of these, however, neither a spectroscopic nor photometric redshift was available from the VVDS database, and we computed ourselves using *Hyperz* (Bolzonella et al. 2000) and the VVDS-SWIRE photometry, as done in Franceschini et al. (2006) and in the GOODS case. Given that none of these 69 sources has a spectroscopic redshift, we are not able to estimate the error in our computed photometric redshift. Clearly, these redshifts are far more uncertain because their corresponding identification are more uncertain. They should be interpreted with care, although luckily their small fraction (4% of the VVDS/SWIRE sample, 2% of the total) does not affect the bulk of our results.

All 1494 sources detected at 24 μm within the optical/NIR/IRAC field have a robust counterpart and redshift. The final sizes of the spectroscopic and photometric redshift samples are 137 and 1357 (9% and 91%), respectively.

3.2. GOODS-S field

The southern GOODS field, or GOODS-S, is arguably on of the most well-studied sky area to date, with deep imaging available from X-ray to radio wavelengths and very extensive spectroscopic follow-up. *Spitzer*, in particular, has very deeply surveyed the GOODS-S field between 3.6 and 8.0 μm using IRAC and over the range 24−160 μm using MIPS.

We used *Spitzer* MIPS 24 μm GOODS-S data products publicly released by the Spitzer Science Center as part of the GOODS Spitzer Legacy Data Products Third Data Release (DR3) of November 2005[3]. This public dataset includes a calibrated map and a catalog of 24 μm sources that is reliable and complete to $S(24\ \mu\mathrm{m}) = 80\ \mu$Jy (80% complete, as reported for example by Le Floc'h et al. 2005). The photometry is based

[1] http://cencosw.oamp.fr/

[2] http://www.oamp.fr/people/arnouts/LE_PHARE.html

[3] Spitzer GOODS-S and GOODS-N data products are available at http://data.spitzer.caltech.edu/popular/goods/Documents/goods_dataproducts.html.

on a PSF fitting algorithm, where the SExtractor positions of IRAC 3.6 μm sources are used as input to the MIPS source extraction process. The MIPS 24 μm PSF was generated from isolated sources in the image, and renormalized based on the aperture corrections published in the MIPS Data Handbook (v2.1, Sect. 3.7.5, Table 3.12).

To compile a multiwavelength photometric and spectroscopic catalog for most of the 24 μm sources, we employed a number of publicly available catalogs. We first used GOODS-MUSIC (GOODS Multiwavelength Southern Infrared Catalog, Grazian et al. 2006, hereafter MUSIC), a 14-band multicolor catalog extracted from surveys conducted over the GOODS-S region, described in Giavalisco et al. (2004). The MUSIC catalog has excellent reliability and completeness, and contains a combination of photometric measurements extending from U to 8.0 μm, including U-band data from the ESO 2.2 m WFI and VIMOS, F435W, F606W, F775W, and F850LP ($BViz$) ACS images, the JHK_s VLT data, and *Spitzer* data acquired by the IRAC instrument at 3.6, 4.5, 5.8, and 8.0 μm.

The MUSIC catalog is jointly selected in the z and K_s bands, meaning that a z primary selection is performed, followed by a K_s secondary additional selection. The latter, in any case, adds a limited number of sources to the catalog, so that for most practical purposes it helps to consider the sample as simply z-selected. Based on this joint z/K_s-selection and the positions thus determined, fluxes for each source are available from the MUSIC catalog in all available bands, from the UV to the IRAC 3.6−8.0 μm channels. In the few cases when an IRAC source in the field appeared to be undetected in z or K_s, we adopted the IRAC-selected catalog of Franceschini et al. (2006). Importantly, the MUSIC catalog also includes spectroscopic (when available, in particular from Vanzella et al. 2005 and 2006 and Le Févre et al. 2004) and photometric redshifts for most sources. As shown by Grazian et al. (2006), the quality of the resulting photometric redshifts is excellent, with an rms scatter in $z/(1+z)$ of 0.06 (similar to what we achieved in VVDS/SWIRE) and no systematic offset over the whole redshift range $0 < z < 6$.

The full GOODS-S 24 μm catalog includes 948 sources over an area of about 250 arcmin^2 and is fully reliable and complete to $S(24\,\mu\mathrm{m}) = 80\,\mu$Jy. The MUSIC catalog provides $UBVizJK_s$ + IRAC photometric coverage over a 143.2 arcmin^2 area, but to maximize the size of our 24 μm sample, we extended this by including areas where either J or K coverage was unavailable (albeit with both $UBViz$ and IRAC). The final effective area of our 24 μm catalog is thus 168 arcmin^2, and the final sample contains 666 sources. For each of these, we searched for counterparts in the MUSIC catalog. Given the well-established one-to-one relation between 3.6 and 24 μm sources, and the ability demonstrated by the deep IRAC 3.6 μm observations to identify even the deepest 24 μm sources (see e.g., Rodighiero et al. 2006), we based our 24 μm identification process on the MUSIC 3.6 μm catalogue.

The likelihood and reliability of the associations were computed using the likelihood ratio (hereafter simply likelihood) technique described by Sutherland & Saunders (1992), whose practical implementation is detailed in Vaccari et al. (2009, in preparation). According to this, the likelihood is defined to be the ratio of the probability that an IRAC 3.6 μm source is the true counterpart to a MIPS 24 μm source to the probability that the association is instead with a nearby background source, based on the assumption that magnitudes and positions are not correlated (i.e., no constraint is based on the source/association flux ratio).

For each 24 μm source, we considered all 3.6 μm sources within a search radius of 5 arcsec as potential counterparts. This is approximately 3 times the quadratically summed rms radial positional errors of MIPS and IRAC sources, which are estimated to be 1.5 and 0.75 arcsec rms, respectively. These values are a little larger than generally assumed but believed to be reasonable given that at these flux limits we are assume that the formal positional errors do not account for confusion effects. The likelihood and reliability values are thus determined by the source number counts of the association catalogue and the source-target relative positions on the sky.

Likelihood and reliability were then computed for all potential counterparts. Among 666 sources, 499 (75%) were assigned a counterpart and a redshift based on the MUSIC catalog that was both highly probable and reliable (>99%), whereas the remaining 167 (25%) were flagged as requiring additional visual checks (i.e., to have a lower likelihood of being true sources and/or to have lower reliability, or no potential counterpart within the 5 arcsec search radius). We also tried additional likelihood and reliability analyses by considering to the z- and K_s entries of the MUSIC catalog, and verified that these new associations did not produce any substantial changes in assigned optical sources, and therefore did not pursue this any further.

Visual checks helped us to solve or at least explain most of the ambiguities. Occasionally, the MUSIC catalog was found to be seriously affected by confusion, or its z/K_s joint selection missed some clearly detected IRAC 3.6 μm source. In most cases, however, visual checks provided a straightforward identification with a given source, or with a close pair of sources at very similar redshifts and thus likely to be in the process of merging. The remaining cases, representing fewer than 10% of the sources that were generally the most confused, disturbed or faintest, were a challenge to identify clearly, and we had to query a number of different catalogs, as well as develop our own photometric redshift measurement. In these cases, we combined information available from the COMBO17 catalog (Wolf et al. 2004) and our own IRAC 3.6 μm selected catalog (Franceschini et al. 2006) to derive the full optical/NIR/IRAC SED of these 24 μm sources, and determine a reliable redshift running an updated version of *Hyperz*, and following the approach described by Franceschini et al. (2006).

Among the 167 (25%) ambiguous cases above, 59 (9%) were assigned a robust counterpart and redshift from the MUSIC catalog following visual checks, 56 (8%) from the COMBO17 catalog, and 32 (5%) from the Franceschini et al. (2006) catalog, leaving only 20 sources, or just 3% of the original sample, without a redshift. All of these extra redshifts were verified and occasionally corrected when reported as unreliable in the original catalogs by running *Hyperz* on the full SEDs.

During this work, when the identification and SED analysis of GOODS-S sources had already been completed, a number of additional spectroscopic redshifts were made available (Ravikumar et al. 2007; Vanzella et al. 2008; Popesso et al. 2009), which Wuyts et al. 2008 compiled into their FIREWORKS catalog. We then adopted the FIREWORKS spectroscopic redshifts for the optical/NIR/IRAC sources that we had previously identified as robust counterparts to 24 μm sources. We used a very stringent 1 arcsec search radius when trying to associate of our MIPS/IRAC/MUSIC sources with the FIREWORKS catalogue, hence obtaining 165 extra spectroscopic redshifts for sources for which only photometric redshifts were previously available, greatly enhancing to the overall quality of our final sample.

Eventually, among the 666 sources detected at 24 μm within the ACS+IRAC field, 646 (97%) sources were assigned a robust counterpart and redshift, leaving only 20 (3%) unidentified

sources. The final numbers of spectroscopic and photometric redshifts are 415 and 231 (64% and 36%), respectively.

3.3. GOODS-N Field

The northern GOODS field, or GOODS-N, was observed by both HST ACS and *Spitzer* IRAC and MIPS to virtually the same depths and over similar areas as GOODS-S, thus providing a useful comparison when evaluating cosmic variance and improving the statistics at faint flux levels. Extensive spectroscopic surveys and multiwavelength optical-to-IR photometry have been provided by Capak et al. (2004), Cowie et al. (2004) and Barger et al. (2008). In this work we have made use for our primary selection of the *Spitzer* MIPS 24 μm GOODS-N data products publicly released by the Spitzer Science Center as part of the GOODS *Spitzer* Legacy Data Products Interim Data Release 1 (IDR1) in February 2004. To perform a multiwavelength identification and SED fitting of the 24 μm sources as described in the previous subsection, we used an original catalog containing all availablel photometric information (U from MOSAIC at KPNO-4-m, $BViz$ from ACS, JHK_s from FLAMINGOS at KPNO 4 m, IRAC channels), as well as a detailed compilation of spectroscopic and photometric redshifts (Mancini et al. 2009). After removing 5σ outliers of the best-fit solution, Mancini et al. found a combined mean offset of $(z_{spec} - z_{phot})/(1 + z_{spec}) = 0.004$ and a rms scatter of $\sigma\,[(z_{spec} - z_{phot})/(1 + z_{spec})] = 0.09$.

This comparison catalog was selected in the IRAC 4.5 μm band, which provides image quality and depth similar to IRAC 3.6 μm. This pure IRAC selection reduces the source confusion problems associated with to a z- or K_s-selected comparison sample: on the one hand, most of the disturbed z/K_s source pairs appear to be unresolved in IRAC images, whereas on the other because some extremely faint z/K_s sources are more robustly detected at IRAC wavelengths, both factors contribute to produce an easier identification process.

We thus carried out a likelihood and reliability analysis of associations between the 24 μm and 4.5 μm sources in the same way as it was described in the previous section, but the number of ambiguous identifications was now extremely low. We also verified that using the IRAC 3.6 μm and IRAC 4.5 μm comparison samples for identification purposes produced virtually identical results.

Among the 904 24 μm sources of the primary selection located within the ACS+IRAC field, only 26 (3%) were flagged for visual checks by the likelihood and reliability criteria outlined in the previous section, and 889 (or 98.3%) sources found a robust counterpart and redshift after the visual checks, leaving only 15 (1.7%) unidentified sources. The final numbers of spectroscopic and photometric redshifts are 290 and 599 (32.5% and 67.5%), respectively.

In Fig. 1, we report the fraction of $S_{24} > 80$ μJy sources with an identified optical counterpart as a function of B, V, i, and z magnitude. The results are presented for both the separate and combined GOODS fields.

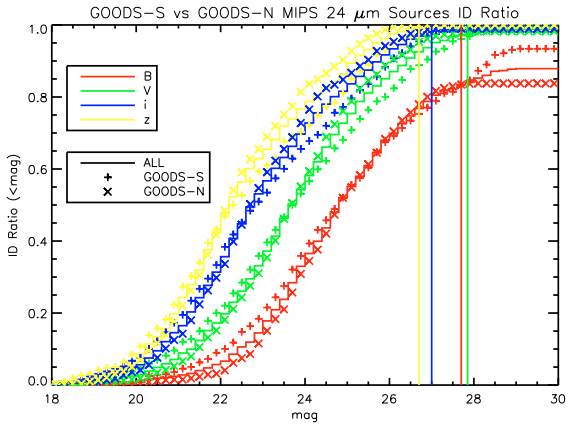

Fig. 1. Fraction of $S_{24} > 80$ μJy sources with an identified optical counterpart as a function of the B, V, i, and z magnitudes. The results are presented for both the separate and combined GOODS-S and GOODS-N fields (see the legend in the figure for details). The vertical lines mark the 5-σ limits of the optical bands.

4. Redshift distribution and source number counts

To characterize the statistical properties of our samples, we present in Fig. 2 the redshift distributions of the 24 μm sources. We compare the two separate distributions of both GOODS-N and GOODS-S and the GOODS with VVDS-SWIRE source samples at the respective flux limits of $S(24\ \mu\text{m}) > 80$ μJy and $S(24\ \mu\text{m}) > 400$ μJy. As is apparent in the figure, our final source sample not only guarantees excellent statistics over the $0 < z < 1.5$ redshift interval, but also include substantial statistical coverage of the high redshift population, up to $z \sim 3$, which is a novelty of the *Spitzer* mission for cosmology compared to the previous ISO surveys. In Fig. 3, we also compare the distributions for the two GOODS fields with the distribution from Le Floc'h et al. (2009), which is based on a large 24 μm sample covering an area of 2 square degrees in the COSMOS field at the same flux level of our GOODS survey (i.e., 80 μJy). The three distributions were normalized to the same sky area of 1 square degree. The COSMOS distribution was renormalized to the GOODS area. The error bars of Le Floc'h et al. account for the effects of cosmic variance, illustrating that the combined use of the two GOODS sky areas is very helpful for reducing the effects of local inhomogeneities. In Fig. 4 we again show the combined redshift distribution for the GOODS-S & GOODS-N fields, this time splitted at different flux levels and compared with the model of Franceschini et al. (2009).

The impact of cosmic variance in our work can also be verified by examining the extragalactic source number counts in the various subsamples that we use. This is presented in Fig. 5, where we show the 24 μm differential number counts in the GOODS-S, GOODS-N, & VVDS-SWIRE fields, separately, and compared with predictions from the Franceschini et al. (2009) model, and previous measurements by Chary et al. (2004), Papovich et al. (2004), and Shupe et al. (2008). We observe general agreement between the various surveys, apart from GOODS-S below $S(24\ \mu\text{m}) < 0.5$ mJy for which the counts are below the other data-set. A similar trend can be also observed in the redshift distribution (Fig. 2, top panel) and later in the 24 μm luminosity function (Fig. 7) and should be attributed to cosmic variance effects.

5. Infrared luminosities from multiwavelength SED fitting

The rich multiwavelength optical-to-IR dataset available in the GOODS and VVDS-SWIRE fields is ideal for performing a spectral fitting procedure on the entire observational SED of each source in our sample. This is needed to calculate the K-corrections to estimate the rest-frame luminosities at different frequencies and the IR bolometric corrections. Since we already know the redshift of each object from the spectroscopic

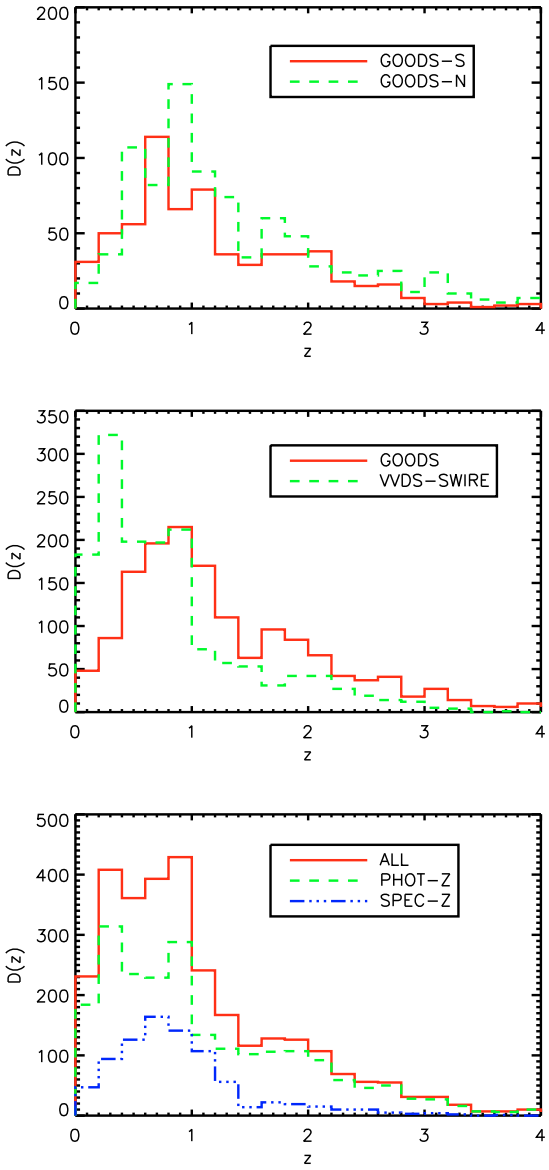

Fig. 2. Observed redshift distributions in our surveys in 0.2 redshift bins. *Top panel*: the separate distributions in the two GOODS fields. *Middle panel*: distributions in the GOODS and VVDS-SWIRE fields. *Lower panel*: continuous line: the redshift distribution for the total sample; dot-dashed line: spectroscopic redshifts; dashed line: photometric redshifts.

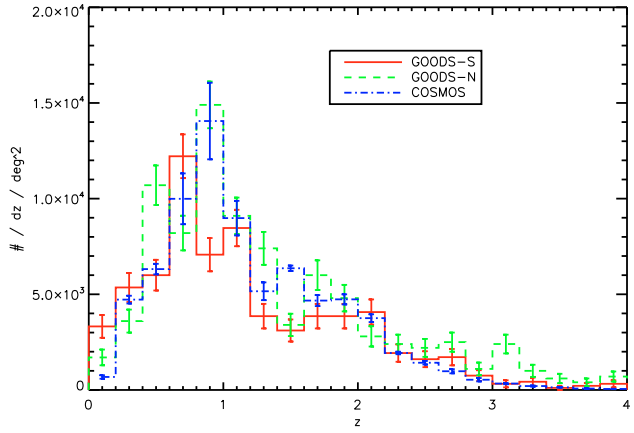

Fig. 3. The separate redshift distributions in the two GOODS fields are compared with the distribution from Le Floc'h et al. (2009), that is based on a large 24 μm sample covering an area of 2 square degrees in the COSMOS field at the same flux level of our GOODS survey, $S(24) > 80$ μJy. The error bars of Le Floc'h et al. account for the effects of cosmic variance.

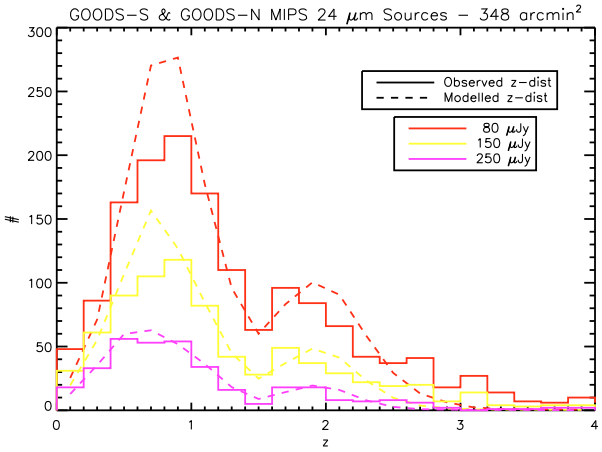

Fig. 4. Combined redshift distribution in GOODS-S and GOODS-N fields. This is shown at different flux levels and compared with the model of Franceschini et al. (2009).

or photometric measurement, we used *Hyperzspec* (Bolzonella, private communication), an updated version of *Hyperz* that performs SED fitting at a fixed redshift, across the whole broad-band photometric set available to us. In this fitting procedure, we compared the optical-to-IR SEDs of 24 μm sources with a library of template SEDs of local objects. The library contains 20 spectra, including one elliptical, seven spirals, three starbursts, six AGNs, and three composite (starburst + AGN) templates covering the wavelength range between 1000 Å and 1000 μm (for a detailed description, see Polletta et al. 2007; and Franceschini et al. 2005). *Hyperzspec* identifies the best-fit SED by minimizing the χ^2 derived by comparing the observed and theoretical SEDs at the redshift of each source.

Given that the restricted library we use cannot be expected to satisfactorily reproduce the observed SED from the UV to the far-IR data of each source, we constrained *Hyperz* to place greater weight on the IR data (e.g. IRAC and MIPS photometric points). We acheived this by artificially changing the photometric errors and providing much smaller values in the *Spitzer* regime. We adopted the following procedure: for optical data (i.e. $\lambda < 1$ μm), we assumed errors of 1 mag, for near-IR data (J, H and K bands) errors of 0.15 mag and for *Spitzer* IRAC and MIPS data errors of 0.1 mag. This combination of weights provided the optimal set of fit to all sources, in general always providing a good description of the mid- to far-IR observed shape of each SED. In this work, a poor fit to the optical side of the spectrum for some sources was not considered to be critical, because we wish to derive luminosities at rest-frame wavelengths above 8 μm. However, the inclusion of the whole SED in the fitting procedure allosw us to fully exploit the photometric information and determine the K-correction in the most reliable way.

This procedure provided a best-fit SED for each galaxy (the few stars were removed a priori on the basis of their optical morphology and/or IR colors) and a rough indication of whether star-formation or AGN-dominated activities are the main source

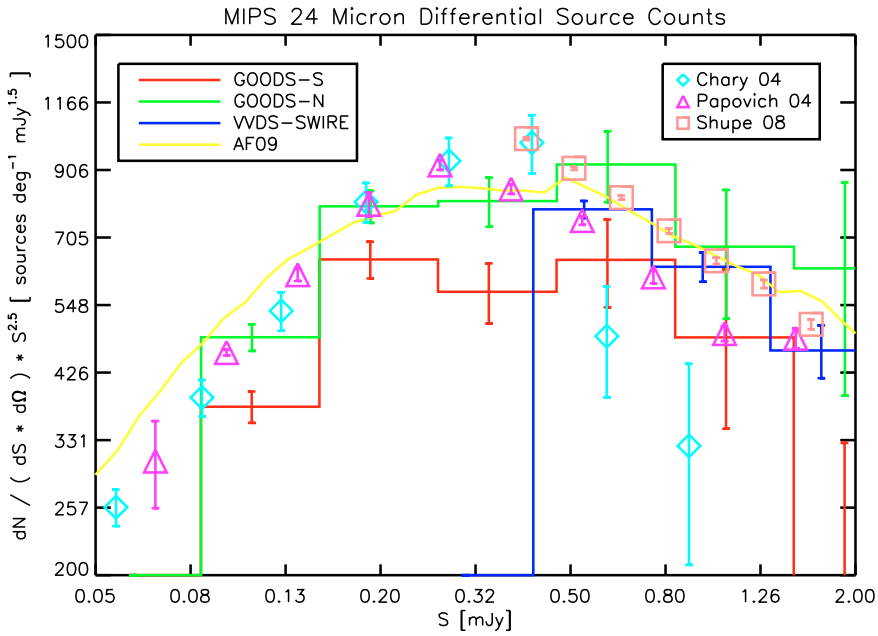

Fig. 5. 24 μm differential number counts in GOODS-S (red histogram), GOODS-N (black histogram) and VVDS-SWIRE (blue histogram) Fields compared with predictions from the Franceschini et al. (2009) model (yellow line), and with previous measurements by Chary et al. (2004), Papovich et al. (2004) and Shupe et al. (2008).

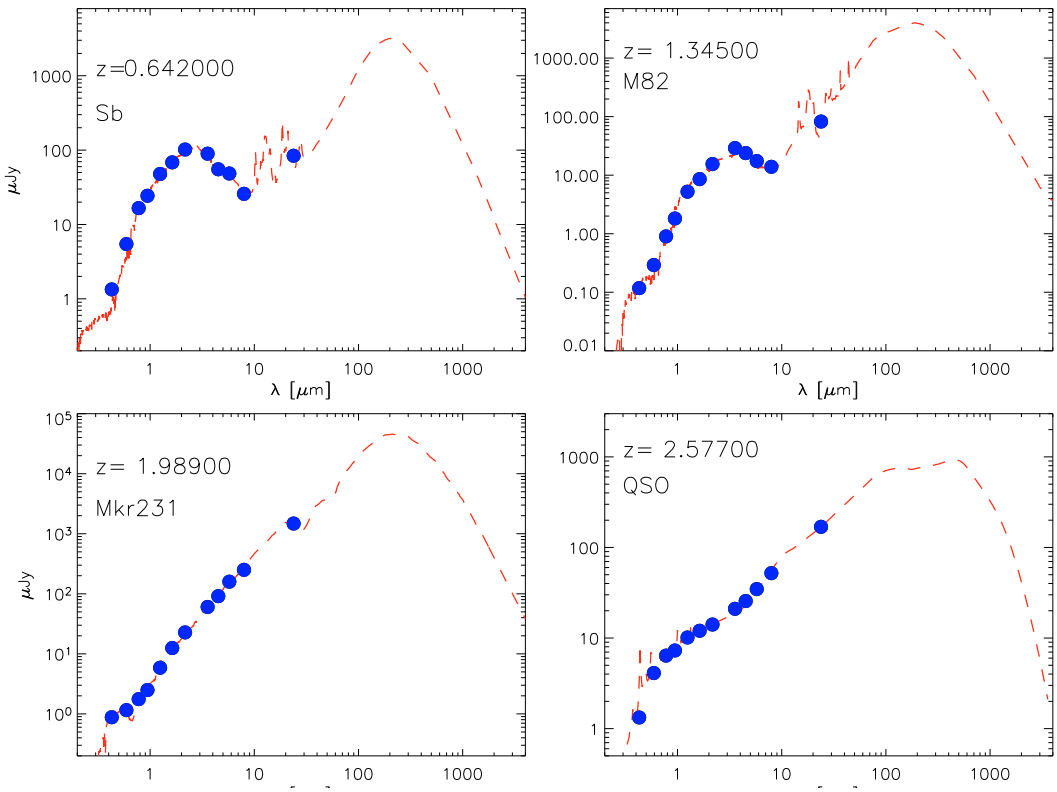

Fig. 6. The observed Spectral Energy Distributions (blue circles) of four sources from our sample, representative of the main spectral classes considered in this work. We also show the best-fit spectra obtained with *Hyperzspec* based on the spectral library by Polletta et al. (2007, red dashed lines). The four SEDs are those of a typical spiral (Sb), a starburst galaxy (M 82), a source whose IR emission is contributed both by star-formation and nuclear activity (Markarian 231) and finally a type-1 quasar (QSO).

of the far-IR emission. As an example, we report in Fig. 6 the best-fits that we obtained for four sources representative of the main spectral classes considered. One of the best-fit solutions is to a typical spiral (Sb) spectrum, another to a starburst galaxy (M 82), to a source whose IR emission is contributed both by star-formation and nuclear activity (Markarian 231), and finally to a type-1 quasar (QSO).

In particular, we identified as type-1 AGN those sources classified by the automatic tool as type-1 quasars or Seyfert-1, corresponding to five SED templates in the Polletta et al. (2007) set. These are characterized by monotonically rising spectra (e.g. Alonso-Herrero et al. 2005), similar to the QSO spectrum in Fig. 6. We found that this class of objects includes 320 sources, or ∼10% of our complete sample. However, this fraction only

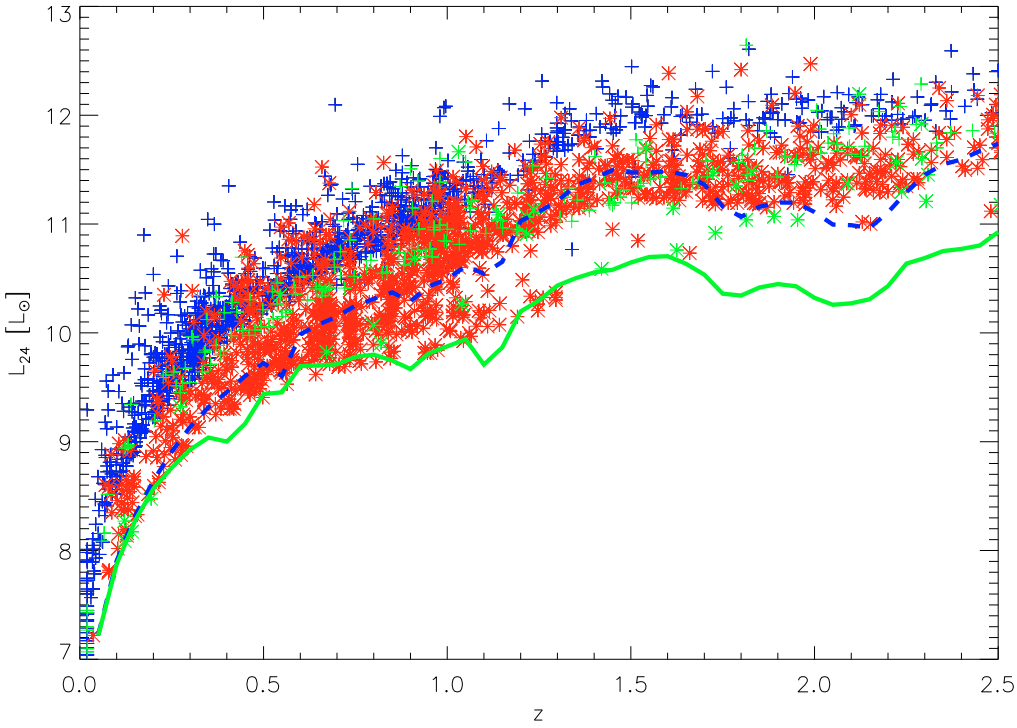

Fig. 7. L_{24} rest-frame 24 μm luminosities as a function of redshift for GOODS (red asterisks) and VVDS-SWIRE (blue crosses) sources. The thick green solid and the blue dashed lines indicate as a function of redshift the 24 μm rest-frame luminosity corresponding to an observed 24 μm flux of 0.08 mJy with the template of an SB galaxy and of M 82, respectively. The green symbols indicate the distribution of type 1 AGNs as selected from the SED fitting procedure.

corresponds to the bright end of our IR LFs, and does not affect our results about their evolution. For this reason, we excluded them from any statistical analysis in the following parts of the paper, such as the computation of the LFs.

The identification of type-2 AGNs or other active sources is far more uncertain, given the complexity of their spectra when they contain mixed contributions from star formation and nuclear activity. The lack of photometric information in the 10−20 μm region of the SED prevented us from being more specific in this classification process in the (majority) case of combined AGN/starburst dust-obscured activity (see also Gruppioni et al. 2008). We defer to future work a more detailed analysis of the AGN luminosity functions, based on the present sample, using color−color diagnostics and X-ray information.

For each source in our combined sample, we calculated the rest-frame NIR and MIR luminosity densities as

$$L_\nu(\nu_{\rm rest}) = \frac{4\pi d_{\rm L}^2}{1+z} S_\nu(\nu_{\rm obs}), \quad (1)$$

where $d_{\rm L}$ is the luminosity distance for a given redshift in our adopted cosmology, S_ν the flux density in erg cm^{-2} s^{-1} Hz^{-1}, and $\nu_{\rm obs}$ and $\nu_{\rm rest}$ are the observed and rest-frame frequencies, respectively, where $\nu_{\rm rest} = (1+z)\nu_{\rm obs}$. Throughout the paper, we present IR luminosities in terms of the bolometric luminosity of the Sun, $L_\odot = 3.83 \times 10^{33}$ erg s^{-1}.

The distribution of 24 μm luminosities as a function of redshift for all sources in GOODS (red symbols) and VVDS-SWIRE (blue symbols) samples are reported in Fig. 7 (type 1 AGNs are marked as green symbols). This figure shows that the combination of the two samples provides a fair coverage in luminosity up to $z \sim 2.5$. To demonstrate the completeness of our survey, we also report as thick green solid and blue dashed lines, as a function of redshift, the 24 μm rest-frame luminosity corresponding to an observed 24 μm flux of 0.08 mJy with the template of an SB galaxy and of M 82, respectively. As can now be clearly seen in Fig. 4, the bimodal distribution in the 24 μm luminosity as a function of redshift is an effect of the K-correction (quiescent spiral versus starburst galaxy).

6. Luminosity functions

A variety of rest-frame wavelengths have been adopted by different authors to infer from *Spitzer* data the redshift evolution of the MIR luminosity functions and to compare them to local functions. Caputi et al. (2007) presented the rest-frame 8 μm LF at $z \sim 1$ and $z \sim 2$, Perez-Gonzalez et al. (2005) derived the rest-frame 12 μm LF up to $z \sim 2.5$, Le Floc'h et al. (2006) obtained the 15 μm LF up to $z \sim 1.2$, and Babbedge et al. (2006) computed the LF at both 8 and 24 μm up to $z \sim 2$, albeit with uncertainties substantially increasing with redshifts arising from their relying on shallow *Spitzer* and optical photometry and on purely photometric redshifts. Some authors also tried to compute the evolutionary IR [8−1000 μm] LF.

Our largely improved sample enables homogeneous selection from a large database, including of data from the wide VVDS-SWIRE field, which are essential for a proper sampling of the high-luminosity end of the LF and minimizing the effects of cosmic variance on the deeper samples. The GOODS samples which are smaller but contain data a factor 5 deeper in flux, $S(24) > 80$ μJy have been shown to tightly constrain the evolution of the LF at lower luminosity levels and higher redshifts (e.g., Caputi et al. 2007; Le Floc'h et al. 2005).

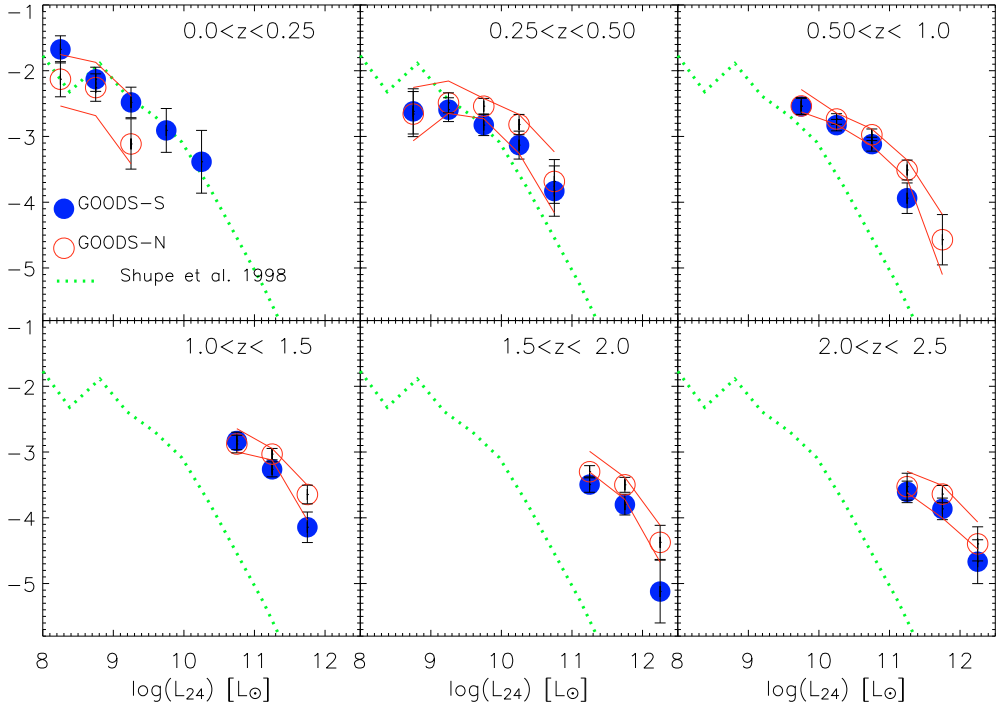

Fig. 8. Rest-frame 24 μm luminosity function for all galaxies in the GOODS-North and GOODS-South separated, as computed with the $1/V_{\rm max}$. As a reference, we report the local luminosity function at 25 μm (dotted green line) by Shupe et al. (1998). The red open circles represent the original estimates of the GOODS-N 24mu LF values, together with their poissonian error bars. The red upper and lower solid lines represent the range of values derived with 100 iterations by allowing a change in photo-z and K-correction.

6.1. LF computation

The LFs at the rest-frame wavelengths of 8, 12, 15, and 24 μm from our combined GOODS+VVDS-SWIRE sample were computed using the $1/V_{\rm max}$ method (Schmidt 1968). The advantage of this technique is that it allows direct computation of the LF from the data, without any parametric dependence or model assumption. We divided the sample into redshift bins selected to ensure an adequate numbers of galaxies in each bins. Our adopted redshift binning was different at different wavelengths, to allow an easier comparison with published data.

Within each redshift bin, the comoving volume of each source was defined to be $V_{\rm max} = V_{z_{\rm max}} - V_{z_{\rm min}}$. The $z_{\rm max}$ value corresponds to the maximum redshift at which a source would still be included in the sample, given the limiting 24 μm flux, while $z_{\rm min}$ is the lower limit to the considered redshift bin. In any case, $z_{\rm max}$ should be lower than the maximum redshift of the bin considered.

As previously mentioned in Sect. 3, all of our 24 μm catalogs are basically complete to our adopted limiting fluxes (at 400 and 80 μJy), and thus we did not apply any completeness correction.

We checked the consistency between the catalogs, within the statistical errors (the error bars include only the Poisson noise), and the effects of cosmic variance in our LF by comparing the results obtained independently in the separate fields. In particular, the rest-frame 24 μm LF calculated from the GOODS-North and in the GOODS-South samples are reported in Fig. 8. The two LFs appear to be consistent with each other within the error bars (as found by Caputi et al. 2007 for their rest-frame 8 μm LF).

To reduce the effects of cosmic variance and to enhance the quality of the statistics, we provide in the following combined results for the three samples.

To quantify the effects of the uncertainties in photometric redshifts and the K-correction on our luminosity functions, we performed a set of Monte Carlo simulations. As a test case, we used the GOODS-N sample, and we checked the effect on the 24 μm luminosity function, which requires the most significant extrapolation of the data. We iterated the computation of the 24 μm LF by varying each time the photometric redshift of each source (by an amount corresponding to the rms in the photo-z/spec-z relation reported for the GOODS-N, i.e., 0.09). Each time, we then recomputed the monochromatic luminosity by performing, as in the main case, the SED fitting with *Hyperz* and the computation of the $V_{\rm max}$. We allow *Hyperz* to choose a new best-fit template, to take simultaneously into account a variation in redshift and K-correction. We also included Arp200 in the library of templates to see if the effect of a more extreme ULIRG does affect our results. The results of this Monte Carlo simulation are also reported in Fig. 8 . The red open circles represent the original estimates of the GOODS-N 24mu LF values, with their Poissonian error bars. The red upper and lower solid lines represent the range of values derived with 100 iterations by allowing a change in photo-z and K-correction. The comparison shows that the combined effects of photometric redshift and K-correction on the error bars are indeed larger than the simple Poissonian values. However, considering the GOODS-S data (blue circles), we seem to find that cosmic variance has a greater impact than the photo-z uncertainties. Given that we cannot reliably estimate the cosmic variance in the full survey (and that we

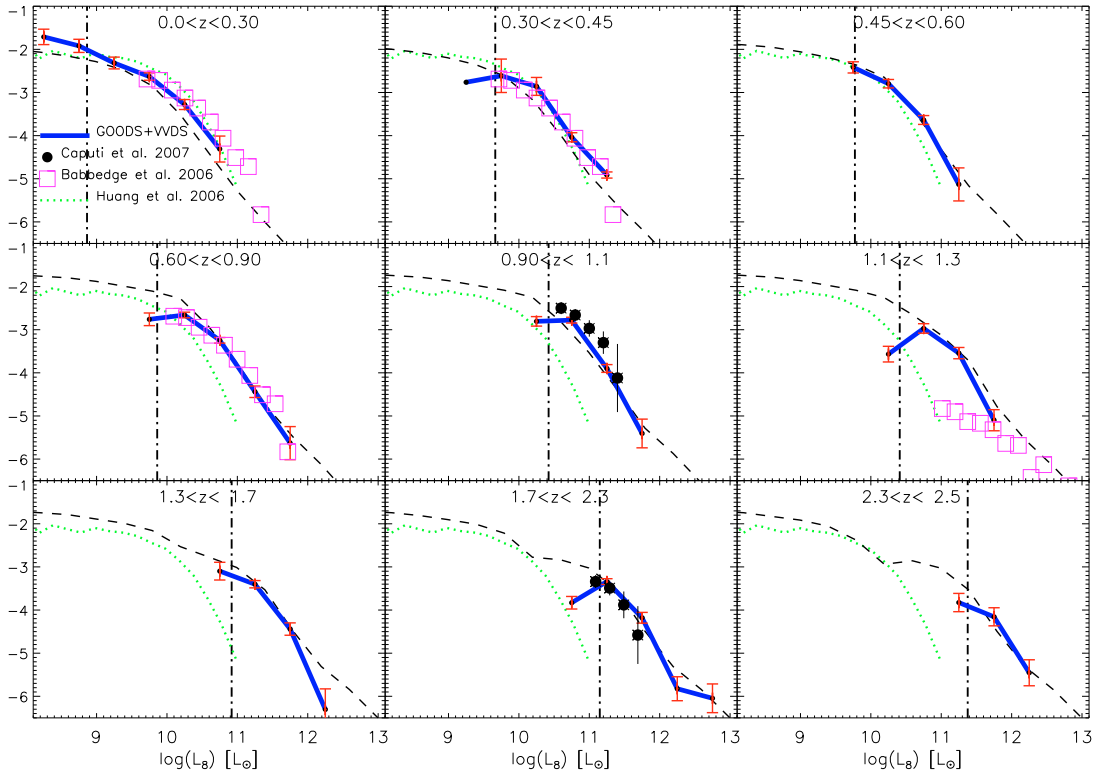

Fig. 9. Rest-frame LF at 8 μm. The blue thick lines mark our combined GOODS+VVDS-SWIRE luminosity functions in the various redshift bins. In each panel we compare our results with literature data (when available). The green-dotted line represents the local LF as computed by Huang et al. (2006). The filled black symbols are from Caputi et al. (2007), while the open pink squares are from the SWIRE survey (Babbadge et al. 2006). The vertical dot-dashed lines reported in each redshift bin represent the luminosity above which we do not expect any incompleteness. We also report as black-dashed lines the model predictions by Franceschini et al. (2009).

are using different fields to help minimize this problem) in this paper, we prefer to use the Poissonian error bars to derive our conclusions.

6.2. Results for various IR bands

In Figs. 9 to 12, we present our rest-frame 8, 12, 15, and 24 μm luminosity functions, respectively. As mentioned above, the choice of redshift bins is different for different wavelengths, depending on the available published data with which we comparise. The redshift and luminosity binning is also constrained to ensure that a statistically sufficient number of sources can be studied. The error bars represent only Poisson noise. The vertical dot-dashed lines reported in each redshift bin represent the luminosity above which we do not expect any incompleteness. This is clearly evident from the data themselves, which begin to decline below this level, mainly because at fainter luminosities not all galaxy types are observable (depending on their SED, see Ilbert et al. 2004 for a detailed discussion of this bias). The center of each luminosity bin has been computed as the median of the observed luminosities distribution in the corresponding bin. The LFs from the total combined GOODS+VVDS-SWIRE, including all galaxy types, are reported in each figure panels with a thick blue line. The values of the monochromatic LFs at 8, 12, 15, and 24 μm are also reported in Tables 1–4, respectively.

Our results in Figs. 9 to 12 are compared with available data in the literature, whenever available. At 8 μm (Fig. 9), the most significant comparison is with the results of Caputi et al. (2007), who computed the rest-frame LF at $z \sim 1$ and $z \sim 2$ from the combined dataset in GOODS-S and GOODS-N. We find fairly good agreement within the errorbars, although some differences exist, in the two redshift bins and reach similar luminosity levels of completeness. However, the addition of the VVDS-SWIRE data allows us to extend the LF to higher luminosities. This result might confirm the finding of Caputi et al. that different ways of estimating the K-correction provide consistent results when deriving the monochromatic IR luminosity functions at high-z. To $z \sim 1$, we also find good consistency with the results of Babbedge et al. (2006) which were based on the SWIRE survey. However, this results at higher z significantly differ from ours, the LF being much lower.

At 12 μm (Fig. 10), a valuable comparison is possible to $z \sim 2.5$ with the LF derived by Perez-Gonzalez et al. (2005), which was based on a large sample of more than 8000 sources brighter than $S(24\ \mu\text{m}) = 80\ \mu$Jy. Although this work is based purely on photometric redshifts, we observe general good agreement with our estimates to $z \sim 1.8$ in terms of the bright-end of the LFs, while we note that our LFs seem to be lower in the fainter luminosity bins computed from our data. In the two higher redshift bins ($1.8 < z < 2.2$ and $2.2 < z < 2.6$), the LF values observed in our case are systematically lower, a difference that is probably caused by a combination of uncertainties in the photometric redshifts and in the K-corrections, and to cosmic variance.

Similar conclusions can be drawn about the 15 μm results (Fig. 11), where the major reference comes from

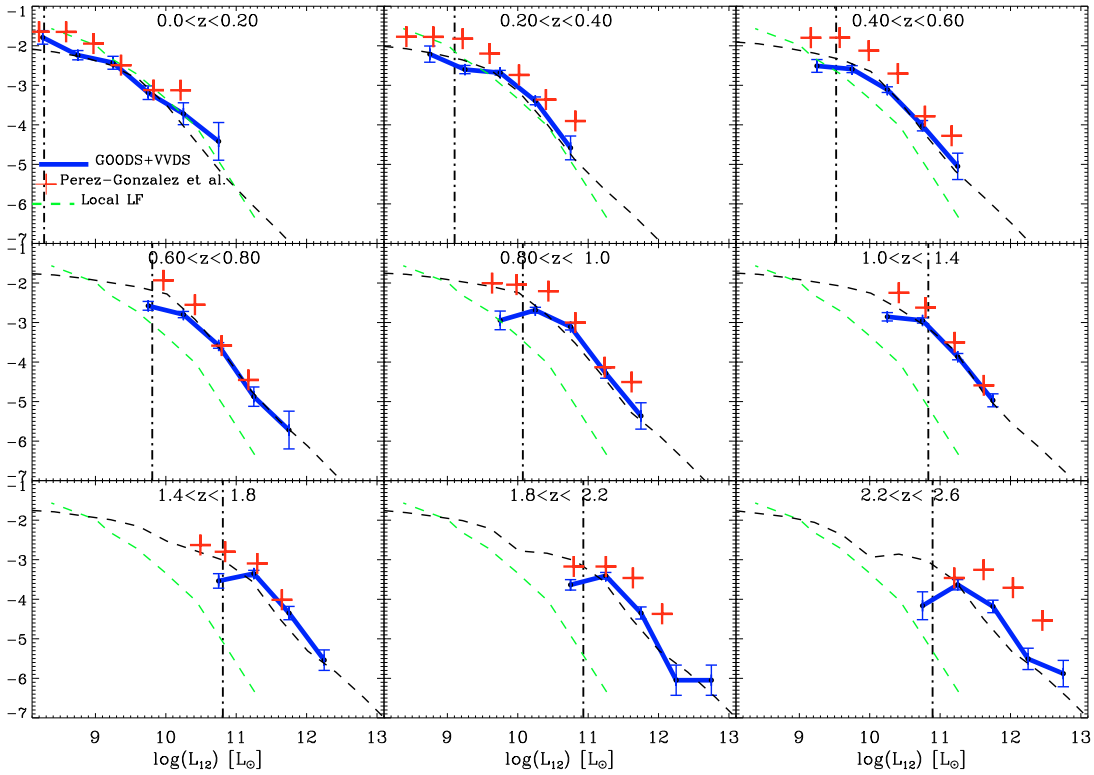

Fig. 10. Rest-frame LF at 12 μm. The blue thick lines mark our combined GOODS+VVDS-SWIRE luminosity functions in the various redshift bins. In each panel, we compare our results with literature data (if available). The green-dashed line represents the local LF (Rush et al. 1993). The red-crosses are from Perez-Gonzalez et al. (2005). The vertical dot-dashed lines reported in each redshift bin represent the luminosity above which we do not expect any incompleteness. We also report as black-dashed lines the model predictions by Franceschini et al. (2009).

Le Floc'h et al. (2005) LF estimation up to $z \sim 1$. We also present the results of Magnelli et al. (2009) to $z \sim 1$ (we report their best-fit double power-law). In this case, our combined GOODS+VVDS-SWIRE sample provides consistent results in the common redshift range. A comparison is also shown with the local LF derived by Pozzi et al. (2004).

Finally, we attempted to compute for the first time the rest-frame 24 μm LF to $z \sim 2.5$. The results are presented in Fig. 12. A comparison can be performed at low redshifts with both the IRAS 25 μm LF (Shupe et al. 1998) and the *Spitzer* results from the First Look Survey (FLS) 24 μm team (Marleau et al. 2007). As observed at 8 μm, the LF computed by Babbedge et al. (2006) is consistent with our results at 24 μm to $z \sim 1$. Above, their values seem to underestimate the present computation. We also show the estimate by Vaccari et al. (2009) based on the SWIRE-SDSS database. We note the close agreement between our estimate of the $z < 0.3$ LF and the local ones.

6.3. Total infrared bolometric luminosities and LF

Much efforts has been made by various authors to convert the observed MIR luminosities into total infrared (TIR) luminosities (e.g., Chary & Elbaz 2001; Elbaz et al. 2002; Takeuchi et al. 2005; Caputi et al. 2007; see Bavouzet et al. 2008, and references therein for a review). There is obvious strong interest in attempting to estimate both the bolometric luminosities of cosmic sources and the evolution of the bolometric luminosity functions, because these quantities can be directly scaled to the rates of gas processing into stars (Kennicutt 1983; Rowan-Robinson et al. 1997), for the stellar-dominated, and of gas nuclear accretion, for the AGN-dominated objects. Based on studies of the spectral energy distributions of local sources, these corrections to (our reference) 24 μm fluxes are relatively well established (e.g., Caputi et al. 2007; Bavouzet et al. 2008).

Our adopted procedure in the present paper has been to integrate for each object the best-fit SED, which we obtained in Sect. 5, in the rest-frame [8−1000 μm] interval, as a measure of the corresponding TIR luminosity. The result of this computation is shown in Fig. 13, where we indicate with different symbols the distribution of the TIR luminosities for our GOODS and VVDS-SWIRE sources, as a function of redshift. Our approach is similar to others in the literature (Le Floc'h et al. 2005; Perez-Gonzalez et al. 2005; Caputi et al. 2007), which all use similar sets of templates of local IR galaxies to fit the data. As in Fig. 3, the thick green solid and blue dashed lines in Fig. 9 indicate, as a function of redshift, the total IR luminosity corresponding to an observed 24 μm flux of 0.08 mJy with the template of an SB galaxy and of M 82, respectively.

To check the consistency of our approach, we compared our results with those of Takeuchi et al. (2005), Sajina et al. (2005), Caputi et al. (2007), and Bavouzet et al. (2008), in particular. In their work, Caputi et al. provide an empirical calibration of the conversion from $\nu L_\nu(8\ \mu\mathrm{m})$ to the bolometric IR luminosity ($L^{\mathrm{IR}}_{\mathrm{bol}}$), based on a sample of *Spitzer*-selected galaxies, while Takeuchi et al. (2005) and Sajina et al. (2005) obtain a relation between $\nu L_\nu(24\ \mu\mathrm{m})$ and $L^{\mathrm{IR}}_{\mathrm{bol}}$. Bavouzet et al. (2008) elaborate on the latter by including into the analysis, data at 8, 24, 70 and 160 μm, mostly from *Spitzer*, for their sample sources. These

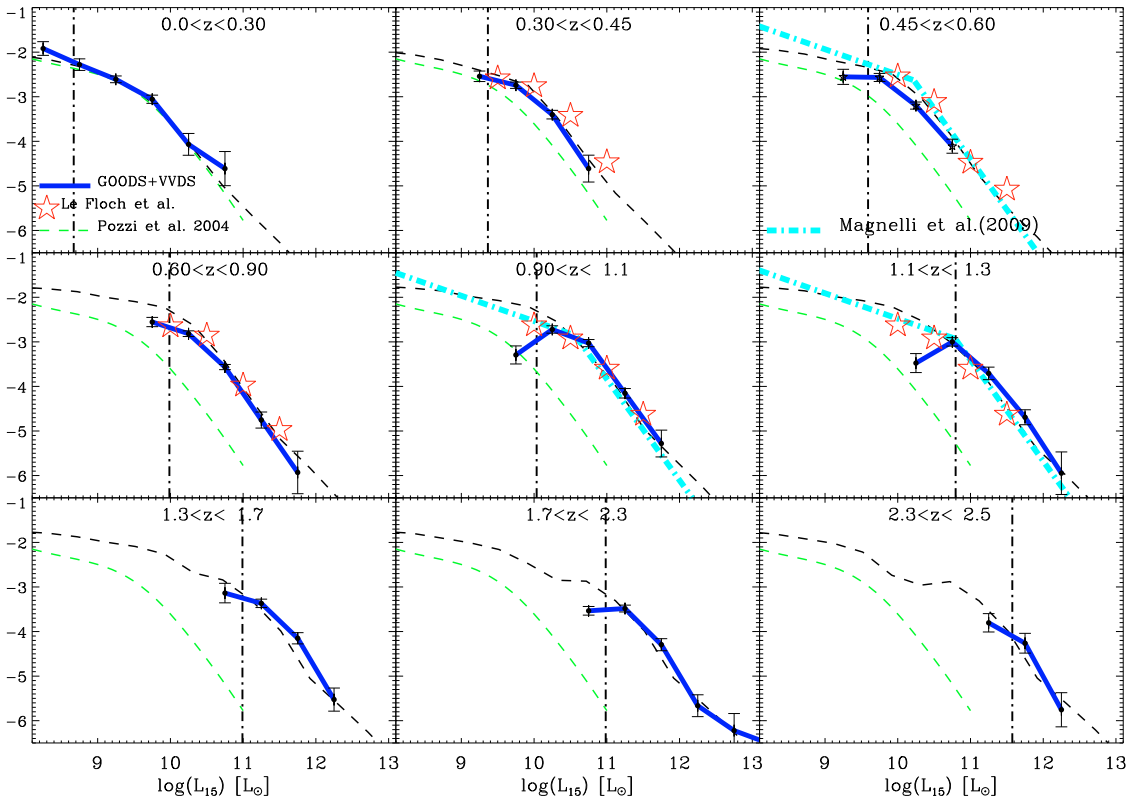

Fig. 11. Rest-frame LF at 15 μm. The blue thick lines mark our combined GOODS+VVDS-SWIRE luminosity functions in the various redshift bins. In each panel we compare our results with literature data (if available). Open circles represent the local LF (Pozzi et al. 2004), red-stars are from Le Floc'h et al. (2005) and the cyan dot-dashed lines are from Magnelli et al. (2009). The vertical dot-dashed lines reported in each redshift bin represent the luminosity above which we do not expect any incompleteness. We also report as black-dashed lines the model predictions by Franceschini et al. (2009).

relations should then be reliable up to $z \sim 2$ and $z \sim 1$ for ULIRGs and LIRGs, respectively.

In Fig. 14, we report a comparison of our observed monochromatic versus bolometric relation for all our sample sources with the average adopted relations by Caputi et al. (8 μm; left panel) and Bavouzet et al. (24 μm; right panel). The various datapoint alignments in the plots correspond to the different spectral templates that we used to fit our photometric data.

The solid line in the left panel shows the empirical relation provided by Caputi et al. (2007) for the rest-frame 8 μm wavelength. We observe an excellent agreement between our average relationship and that by Caputi et al. (2007), over the whole luminosity range. The relations provided by Bavouzet et al. (2008) are calibrated using longer wavelength MIPS data (70 and 160 μm) and should be considered as particularly reliable. We report those for the 8 μm and 24 μm (dashed and dot-dashed lines in both panels of Fig. 14, calibrated on local and high-redshift galaxies, respectively). At 8 μm, the relation of Bavouzet et al. appears to be somewhat flatter than ours, but still consistent within the data dispersion. However, we note that when extrapolating the relation at high-z, Bavouzet et al. use the stacking technique, which may produce incorrect faint IR luminosities; their faint total IR luminosities indeed appear to be overestimated compared to our data.

The comparison of the monochromatic 24 μm and bolometric luminosities in the right panel shows good agreement with the relations of Takeuchi et al. (2005) and a slight offset with Sajina et al. (2005). However, the slope of the Bavouzet et al. relation appears to be flatter than ours. This difference suggests a potential underestimate of our TIR luminosities below $\log(L_{\rm IR}) < 10.5\ L_{\odot}$ in the lowest redshift bin ($z < 0.3$). However, given the flatness of the LF at these faint luminosities, even a significant underestimate of the true $L_{\rm IR}$ at these luminosities would not strongly affect our results.

By applying the same method as described in Sect. 6.1 to compute the monochromatic luminosity functions, we derived the bolometric [8−1000 μm] LF to $z \sim 2.5$. The results are presented in Fig. 15 and reported in Table 5.

As we did for the monochromatic LF discussed in Sect. 6.2, we compared our results with those available in the literature, adapting our choice of redshift bins. Again, we find general consistency with other results at various redshifts, in particular with the LF estimates of Le Floc'h et al. (2005), Huynh et al. (2007), and Magnelli et al. (2009) to $z \sim 1$. The latter is based on the *Spitzer* MIPS 70 μm data in the GOODS-N field and should be considered as particularly reliable due to the moderate bolometric correction. At higher redshift, we observe a general agreement with the results published by Caputi et al. (2007) at $z \sim 2$ and some consistency also with the $2 < z < 2.5$ bolometric LF at the extremely high luminosity values derived by Chapman et al. (2005) from radio-detected submillimeter galaxies.

To obtain a visual impression of the observed LF evolution, we report in each panel the local bolometric LF computed by Sanders et al. (2003) for the IRAS revised galaxy sample.

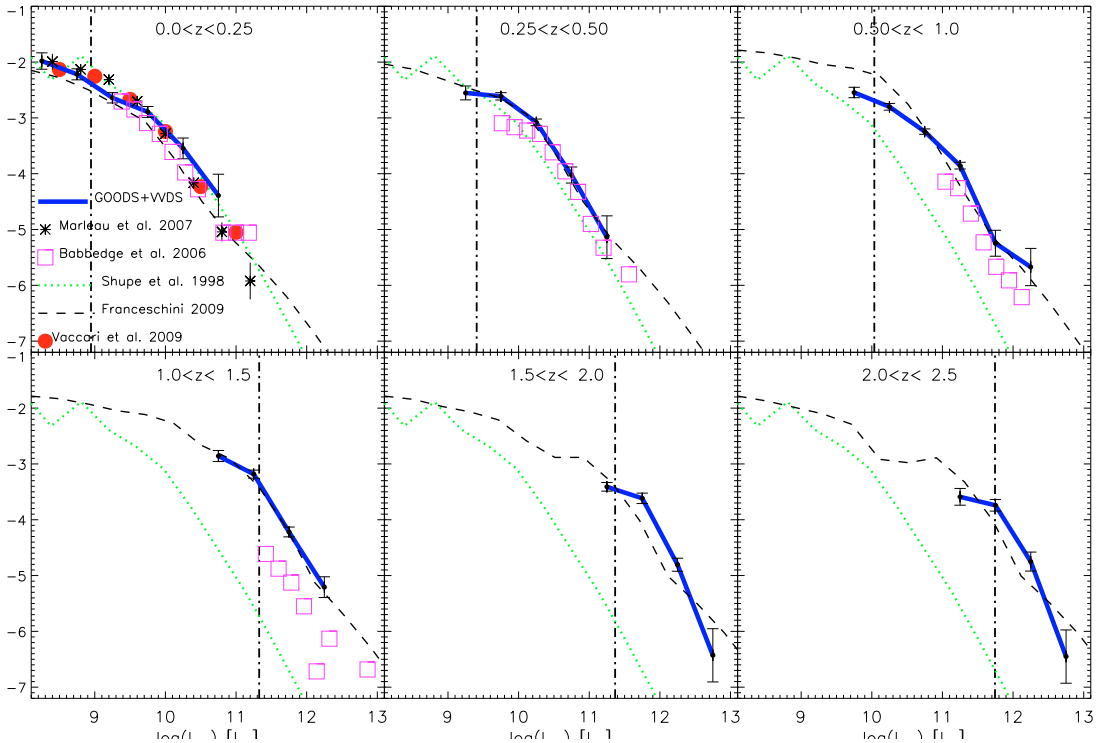

Fig. 12. Rest-frame LF at 24 μm. The blue thick lines mark our combined GOODS+VVDS-SWIRE luminosity functions in the various redshift bins. In each panel we compare our results with literature data (if available). The dotted-green line represents the local LF (Shupe et al. 1998). The black asterisks are the local LF as computed by Marleau et al. (2007), the open pink squares are from the SWIRE survey (Babbedge et al. 2006) and the red filled circle shows a recent estimate by Vaccari et al. (2009) based on the SWIRE-SDSS database. We also report as black-dashed lines the model predictions by Franceschini et al. (2009). The vertical dot-dashed lines reported in each redshift bin represent the luminosity above which we do not expect any incompleteness.

7. Discussion

7.1. The evolutionary bolometric luminosity functions

For an easier description of the evolution of the bolometric LF, we adopted a routinely used parameterization law (Saunders et al. 1990; Pozzi et al. 2004; Le Floc'h et al. 2005; Caputi et al. 2007) to fit our data

$$\Phi(L)\,\mathrm{d}\log_{10}(L) = \Phi^*\left(\frac{L}{L^*}\right)^{1-\alpha} \times\exp\left[-\frac{1}{2\sigma^2}\log_{10}^2\left(1+\frac{L}{L^*}\right)\right]\mathrm{d}\log_{10}(L), \quad (2)$$

where, in this case, L is the TIR [8−1000 μm] luminosity, the parameter α corresponds to the slope at the faint end, L^* is the characteristic $L_{\rm bol}^{\rm IR}$ luminosity, and Φ^* is the normalization factor. The best-fit parameters for the local LF are: $\alpha \simeq 1.2$, $\sigma \simeq 0.7$, $L^* \simeq 1.77\,10^9\,L_\odot$, and $\Phi^* \simeq 0.0089\,\mathrm{Mpc}^{-3}$.

The main uncertainties that may affect our results are those concerning the estimate of the bolometric luminosity from multiwavelength data limited to $\lambda < 24\,\mu$m, and the lack of statistics at the faint end of the LF preventing us from significantly constraining its slope. We kept the slope of the faint-end of the LF fixed to the local observed value ($\alpha = 1.2$; see also Zheng et al. 2006; Caputi et al. 2007) and we fitted the observations in each redshift bin by varying only L^* and Φ^*, using a χ^2 minimization procedure. The slope at the bright end has only been slightly changed manually in a couple of redshift bins to provide a closer fit in the highest luminosity bin. This procedure corresponds to a combination of luminosity and density evolution. The results of the fitting procedure are presented in Fig. 15 (solid black lines).

From our fitting, we infer that the comoving number density of sources, as parameterized by Φ^*, evolves as $(1+z)^{1.1}$ in the redshift range $0 < z < 1$, while the characteristic infrared luminosity (L^*) evolves as $(1+z)^{2.7}$. Above $z > 1$, the degeneracy between luminosity and density evolution becomes more significant because of the narrower range in luminosity covered by our LF. However, the LFs at $z > 1$ are consistent with no or limited evolution.

7.2. The bolometric IR luminosity density

One of the goals for computing the bolometric luminosity functions is to estimate the total comoving IR luminosity density as a function of redshift. This inference has important cosmological implications, because it is tightly related with the evolution of the comoving star formation rate density and the rate of gravitational accretion onto black-holes.

As discussed in many papers based mostly on *Spitzer* data (Yan et al. 2007; Sajina et al. 2007, 2008; Daddi et al. 2007; Fiore et al. 2008; see also Fadda et al. 2002; Franceschini et al. 2005), violent starburst and AGN activities are often concomitant in *Spitzer* 24 μm sources at $z \sim 2$. All these analyses agree that, after excluding the most obvious type-1 AGN, it is not easy to estimate the relative AGN/starburst contributions in high-redshift sources, even including the widest SED coverage and optical/IR spectroscopic data, given the role of dust extinction in

Table 1. 8 μm luminosity function values.

$\log(L_8/L_\odot)$	8.25	8.75	9.25	9.75	10.25	10.75	11.25	11.75	12.25	12.75
$0.00 < z < 0.30$	-1.71 ± 0.18	-1.92 ± 0.15	-2.32 ± 0.14	-2.63 ± 0.08	-3.28 ± 0.12	-4.31 ± 0.30	–	–	–	–
$0.30 < z < 0.45$	–	–	-2.76 ± 0.21	-2.61 ± 0.10	-2.86 ± 0.07	-4.04 ± 0.18	-4.91 ± 0.38	–	–	–
$0.45 < z < 0.60$	–	–	–	-2.42 ± 0.13	-2.80 ± 0.10	-3.64 ± 0.10	-5.13 ± 0.38	–	–	–
$0.60 < z < 0.90$	–	–	–	-2.76 ± 0.15	-2.66 ± 0.07	-3.25 ± 0.07	-4.44 ± 0.13	-5.63 ± 0.38	–	–
$0.90 < z < 1.10$	–	–	–	–	-2.81 ± 0.11	-2.78 ± 0.07	-3.90 ± 0.09	-5.41 ± 0.33	–	–
$1.10 < z < 1.30$	–	–	–	–	–	-2.97 ± 0.11	-3.54 ± 0.13	-5.10 ± 0.24	–	–
$1.30 < z < 1.70$	–	–	–	–	–	-3.10 ± 0.21	-3.40 ± 0.08	-4.44 ± 0.14	-6.31 ± 0.48	–
$1.70 < z < 2.30$	–	–	–	–	–	–	-3.34 ± 0.07	-4.18 ± 0.13	-5.82 ± 0.28	-6.05 ± 0.33
$2.30 < z < 2.50$	–	–	–	–	–	–	-3.83 ± 0.21	-4.16 ± 0.21	-5.45 ± 0.30	–

Notes. The units are $\log(\Phi)$ [Mpc^{-3} dex^{-1}].

Table 2. 12 μm luminosity function values.

$\log(L_{12}/L_\odot)$	8.25	8.75	9.25	9.75	10.25	10.75	11.25	11.75	12.25	12.75
$0.00 < z < 0.20$	-1.79 ± 0.17	-2.24 ± 0.12	-2.43 ± 0.16	-3.19 ± 0.17	-3.72 ± 0.28	-4.42 ± 0.48	–	–	–	–
$0.20 < z < 0.40$	–	-2.21 ± 0.21	-2.60 ± 0.10	-2.68 ± 0.06	-3.39 ± 0.10	-4.58 ± 0.30	–	–	–	–
$0.40 < z < 0.60$	–	–	-2.51 ± 0.16	-2.59 ± 0.09	-3.11 ± 0.07	-4.02 ± 0.13	-5.05 ± 0.33	–	–	–
$0.60 < z < 0.80$	–	–	–	-2.58 ± 0.11	-2.80 ± 0.08	-3.58 ± 0.07	-4.88 ± 0.24	-5.72 ± 0.48	–	–
$0.80 < z < 1.00$	–	–	–	–	-2.69 ± 0.07	-3.11 ± 0.08	-4.28 ± 0.12	-5.36 ± 0.33	–	–
$1.00 < z < 1.40$	–	–	–	–	-2.86 ± 0.11	-2.95 ± 0.07	-3.86 ± 0.08	-4.97 ± 0.16	–	–
$1.40 < z < 1.80$	–	–	–	–	–	-3.54 ± 0.18	-3.35 ± 0.08	-4.35 ± 0.17	-5.54 ± 0.26	–
$1.80 < z < 2.20$	–	–	–	–	–	-3.64 ± 0.13	-3.41 ± 0.08	-4.35 ± 0.15	-6.05 ± 0.38	-6.05 ± 0.38
$2.20 < z < 2.60$	–	–	–	–	–	–	-3.63 ± 0.13	-4.18 ± 0.16	-5.51 ± 0.27	-5.88 ± 0.33

Notes. The units are $\log(\Phi)$ [Mpc^{-3} dex^{-1}].

Table 3. 15 μm luminosity function values.

$\log(L_{15}/L_\odot)$	8.25	8.75	9.25	9.75	10.25	10.75	11.25	11.75	12.25	12.75	13.25
$0.00 < z < 0.30$	-1.92 ± 0.15	-2.28 ± 0.13	-2.61 ± 0.08	-3.06 ± 0.09	-4.07 ± 0.24	-4.61 ± 0.38	–	–	–	–	–
$0.30 < z < 0.45$	–	–	-2.54 ± 0.12	-2.74 ± 0.07	-3.40 ± 0.10	-4.61 ± 0.30	–	–	–	–	–
$0.45 < z < 0.60$	–	–	-2.55 ± 0.17	-2.57 ± 0.09	-3.20 ± 0.08	-4.11 ± 0.16	–	–	–	–	–
$0.60 < z < 0.80$	–	–	–	-2.55 ± 0.10	-2.82 ± 0.06	-3.57 ± 0.06	-4.75 ± 0.18	-5.93 ± 0.48	–	–	–
$0.80 < z < 1.00$	–	–	–	–	-2.72 ± 0.08	-3.03 ± 0.08	-4.15 ± 0.11	-5.28 ± 0.30	–	–	–
$1.00 < z < 1.20$	–	–	–	–	–	-3.00 ± 0.09	-3.71 ± 0.14	-4.69 ± 0.17	-5.95 ± 0.48	–	–
$1.20 < z < 1.70$	–	–	–	–	–	-3.14 ± 0.22	-3.37 ± 0.09	-4.15 ± 0.13	-5.53 ± 0.26	–	–
$1.70 < z < 2.00$	–	–	–	–	–	-3.54 ± 0.10	-3.48 ± 0.08	-4.30 ± 0.14	-5.66 ± 0.25	-6.22 ± 0.38	-6.52 ± 0.48
$2.00 < z < 2.50$	–	–	–	–	–	–	-3.80 ± 0.21	-4.26 ± 0.22	-5.76 ± 0.38	–	–

Notes. The units are $\log(\Phi)$ [Mpc^{-3} dex^{-1}].

Table 4. 24 μm luminosity function values.

$\log(L_{24}/L_{\odot})$	8.25	8.75	9.25	9.75	10.25	10.75	11.25	11.75	12.25	12.75
$0.00 < z < 0.25$	-1.98 ± 0.15	-2.22 ± 0.10	-2.64 ± 0.09	-2.89 ± 0.10	-3.55 ± 0.19	-4.39 ± 0.38	–	–	–	–
$0.25 < z < 0.50$	–	–	-2.55 ± 0.12	-2.61 ± 0.07	-3.08 ± 0.06	-4.02 ± 0.14	-5.14 ± 0.38	–	–	–
$0.50 < z < 1.00$	–	–	–	-2.54 ± 0.09	-2.80 ± 0.06	-3.25 ± 0.05	-3.86 ± 0.06	-5.25 ± 0.23	-5.67 ± 0.33	–
$1.00 < z < 1.50$	–	–	–	–	–	-2.86 ± 0.10	-3.18 ± 0.07	-4.22 ± 0.09	-5.21 ± 0.19	–
$1.50 < z < 2.00$	–	–	–	–	–	–	-3.41 ± 0.08	-3.62 ± 0.09	-4.81 ± 0.12	$-6.4 \pm 3\ 0.48$
$2.00 < z < 2.50$	–	–	–	–	–	–	-3.59 ± 0.15	-3.74 ± 0.10	-4.75 ± 0.17	$-6.4 \pm 5\ 0.48$

Notes. The units are $\log(\Phi)$ [Mpc^{-3} dex^{-1}].

Table 5. Total IR (bolometric) luminosity function values.

$\log(L_{\mathrm{IR}}/L_{\odot})$	8.75	9.25	9.75	10.25	10.75	11.25	11.75	12.25	12.75	13.25	13.75
$0.00 < z < 0.30$	-1.67 ± 0.19	-1.93 ± 0.15	-2.17 ± 0.10	-2.51 ± 0.08	-2.90 ± 0.08	-4.07 ± 0.24	-4.61 ± 0.38	–	–	–	–
$0.30 < z < 0.45$	–	–	–	-2.65 ± 0.16	-2.56 ± 0.08	-3.34 ± 0.09	-4.52 ± 0.28	–	–	–	–
$0.45 < z < 0.60$	–	–	–	–	-2.36 ± 0.12	-2.89 ± 0.10	-4.05 ± 0.15	–	–	–	–
$0.60 < z < 0.80$	–	–	–	–	-2.72 ± 0.14	-2.64 ± 0.07	-3.72 ± 0.09	-4.94 ± 0.26	$-5.7 \pm 2\ 0.48$	–	–
$0.80 < z < 1.00$	–	–	–	–	–	-2.64 ± 0.08	-3.27 ± 0.08	-4.54 ± 0.16	$-5.3 \pm 6\ 0.33$	–	–
$1.00 < z < 1.20$	–	–	–	–	–	-2.83 ± 0.10	-3.05 ± 0.09	-4.28 ± 0.13	$-5.6 \pm 2\ 0.38$	–	–
$1.20 < z < 1.70$	–	–	–	–	–	–	-2.97 ± 0.11	-3.46 ± 0.08	$-4.4 \pm 9\ 0.10$	-5.92 ± 0.33	–
$1.70 < z < 2.00$	–	–	–	–	–	–	-3.45 ± 0.10	-3.54 ± 0.11	$-4.4 \pm 3\ 0.20$	-5.61 ± 0.30	–
$2.00 < z < 2.50$	–	–	–	–	–	–	–	-3.61 ± 0.09	$-4.4 \pm 8\ 0.14$	-6.09 ± 0.39	-6.15 ± 0.38

Notes. The units are $\log(\Phi)$ [Mpc^{-3} dex^{-1}].

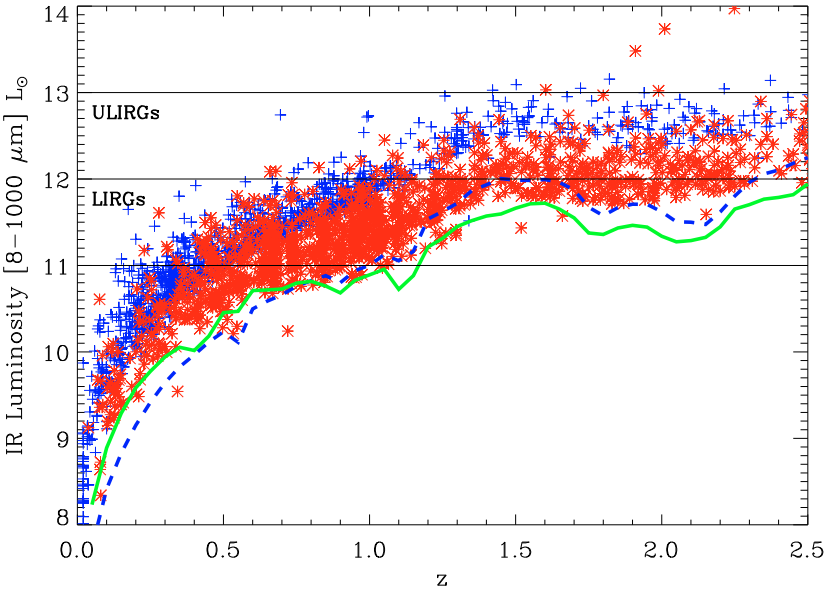

Fig. 13. Total IR luminosities as a function of redshift for GOODS (red asterisks) and VVDS-SWIRE (blue crosses) sources. The thick green solid and the blue dashed lines indicate as a function of redshift the total IR luminosity corresponding to an observed 24 μm flux of 0.08 mJy with the template of an SB galaxy and of M 82, respectively.

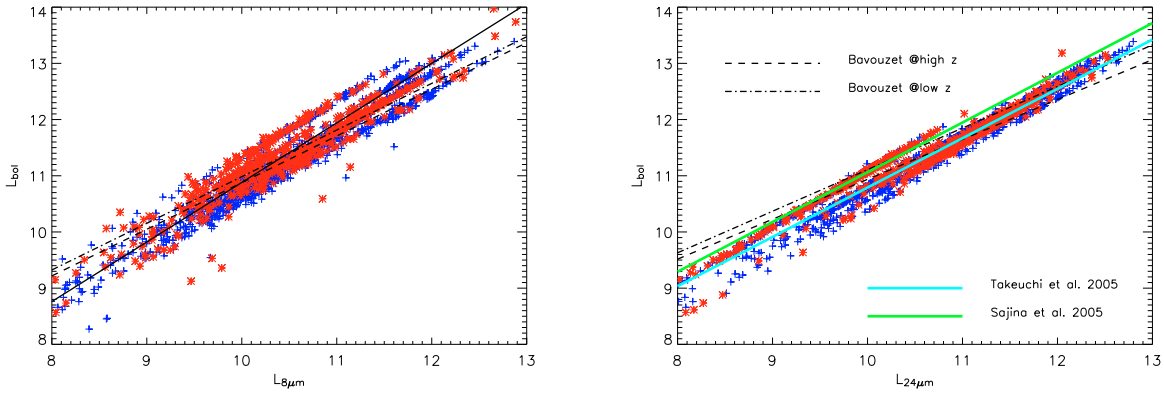

Fig. 14. Distribution of total IR luminosities as a function of the corresponding monochromatic rest-frame 8 (*left panel*) and 24 μm (*right panel*) luminosities for GOODS (red asterisks) and VVDS-SWIRE (blue crosses) sources. The solid line in the *left panel* shows the empirical relation provided by Caputi et al. (2007) for the rest-frame 8 μm wavelength. The relations provided by Bavouzet et al. (2008) are reported in both panels as dashed and dot-dashed lines (calibrated for local and high-redshift galaxies, respectively). The cyan and green lines show the relations by Takeuchi et al. (2005) and Sajina et al. (2005), respectively.

hiding the primary energy source and the very limited diagnostic power of dust re-radiated spectra.

For this reason, the only attempt that we have made to determine the AGN contribution in our estimate of the luminosity density was to account for the type-1 quasar contribution, whose power source we can attribute entirely to gravitational accretion. Although we might expect that a significant number of the most luminous 24 μm sources should include some fractional AGN contribution, it is likely that the bolometric luminosity of the bulk of the population is dominated by stellar processes (e.g., Ballantyne & Papovich 2007). In any case we account for the AGN-dominated sources in our later analysis.

By integrating the best-fit LF in each redshift bins, shown in Fig. 15, we obtained our determination of the total IR luminosity density up to $z \sim 2.5$, which is reported in Fig. 16 as blue filled squares and tabulated in Table 6. In addition to the Poisson noise, the errorbars that we associated with our estimates account for two major sources of uncertainties: the slope of the faint end of the luminosity function (which was set to be $\alpha = 1.2$ with an error inferred from fitting the local LF), and the error in the normalization parameter (Φ^*) in the χ^2 minimization procedure.

Within the previously mentioned uncertainties, we find general agreement with previously published results based on IR data. The orange filled region in Fig. 16 shows the results of Le Floc'h et al. (2005) to $z \sim 1$, the light pink area marks the data obtained by Caputi et al. (2007) and the magenta curve those by Perez-Gonzalez et al. (2005). In the redshift range $0 < z < 1$, we find that the total bolometric IR luminosity density evolves as $(1 + z)^{3.8\pm0.4}$. This evolution is very close to that derived by Le Floc'h et al. (2005), who found that $(1 + z)^{3.9}$ between $z = 0$ and $z = 1$, but is significantly steeper than estimated by Caputi et al. (2007), $(1 + z)^{3.1}$. At higher redshifts, our results suggest a flattening of the IR luminosity density above $z \sim 1$. The results from the IR data are also in fully agreement within what is derived from the far-ultraviolet data: a strong increase up to $z \sim 1$, and a flatting above as shown for example in Tresse et al. (2007).

We also report in Fig. 16 the separate contributions from LIRGs (here defined as objects with $10^{11} < L_{IR} < 10^{12}\ L_\odot$,

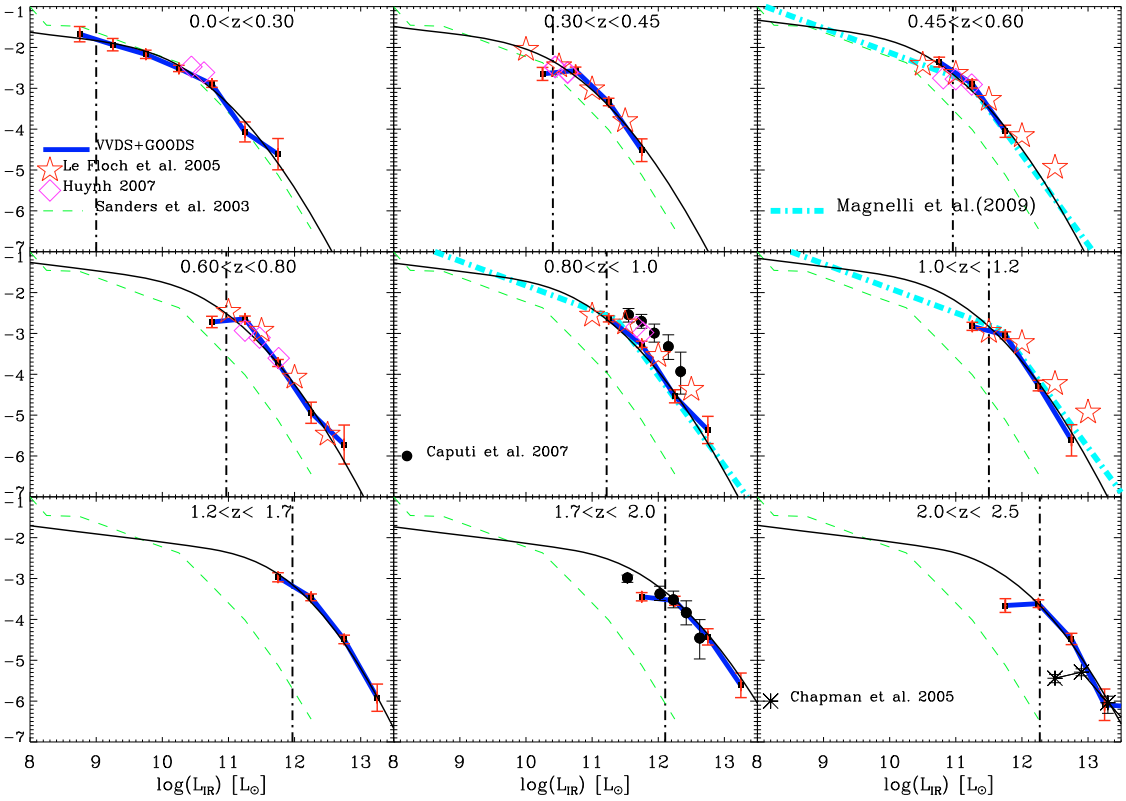

Fig. 15. Bolometric IR (8−1000 μm) LF. The points connected by blue thick lines mark our combined GOODS+VVDS-SWIRE luminosity functions in the various redshift bins (here error bars are plotted in red for clarity). The black solid lines show our best-fit using a parameterized function. In each panel we compare our results with literature data (if available). The dashed-green line represents the local LF as computed by Sanders et al. (2003). The open-pink diamonds are from Huynh et al. (2007), while the open-red stars are from Le Floc'h et al. (2005). The cyan dot-dashed lines are from Magnelli et al. (2009). We also report with black-filled circles the results of Caputi et al. (2007) and with black asterisks the data by Chapman et al. (2005).The vertical dot-dashed lines reported in each redshift bin represent the luminosity above which we do not expect any incompleteness.

green dashed line) and ULIRGs ($L_{\rm IR} > 10^{12} L_{\odot}$, red dot-dashed line) to the IR luminosity density. At $z \sim 0.2$, ~30% of the bolometric IR luminosity density is contained in LIRGs and <1% in ULIRGs. At $z = 1$, we find that LIRGs and ULIRGs contribute 45% and 6%, respectively, to the total IR luminosity density. At $z \sim 2$, the contributions of LIRGs and ULIRGs become 48% and 45% of the total budget, respectively: the cosmic evolution of the highest- and of the moderate-luminosity sources appear to be drastically different. This finding is consistent with the results of previous *Spitzer* studies of the specific SF for star-forming galaxies (e.g. Perez-Gonzalez et al. 2005; Santini et al. 2009).

Finally, we estimated the comoving luminosity densities after removing the contribution of the 180 sources identified as type-1 AGNs from our SED fitting, as explained in Sect. 5. However, this does not make any significant difference in Fig. 16. Assuming that the remaining part of the population has a bolometric emission dominated by star formation, we report on the right-hand ordinate axis of Fig. 16 the comoving SFR density, which we calculate from Kennicutt et al. (1998): $SFR[M_{\odot}/\mathrm{yr}] = 1.7 \times 10^{-10}\ L([8{-}1000\,\mu\mathrm{m}])/L_{\odot}$.

7.3. Evolution of the comoving source space density

A more detailed inspection of the evolutionary properties of the IR selected sources is presented in Fig. 17 in terms of the variation with redshift of the comoving source space densities for different IR luminosity classes. The data points were derived from the best-fit to the bolometric LFs shown in Fig. 15, but we report only the data within luminosity intervals acceptably constrained by our observations.

Table 6. Bolometric IR luminosity density values as a function of redshift.

z	$\rho_{\rm IR}(L_{\odot}\ \mathrm{Mpc}^{-3})/10^8$
0.150	$1.18^{+0.36}_{-0.37}$
0.375	$2.17^{+0.84}_{-0.50}$
0.525	$4.04^{+1.34}_{-1.17}$
0.700	$5.51^{+2.21}_{-1.47}$
0.900	$7.39^{+2.22}_{-1.57}$
1.100	$11.33^{+2.27}_{-3.78}$
1.500	$11.99^{+3.16}_{-4.70}$
1.850	$12.23^{+6.16}_{-6.00}$
2.250	$11.21^{+4.28}_{-5.93}$

The figure indicates a systematic shift with redshift of the number density peak as a function of luminosity: the brightest IR galaxies formed earlier in the cosmic history ($z > \sim 1.5$), while the number density of the less luminous ones peaks at lower redshifts ($z \sim 1$ for $L_{\rm IR} \leq 10^{11}$). Although our results do not constrain the high-redshift evolution of the lower luminosity

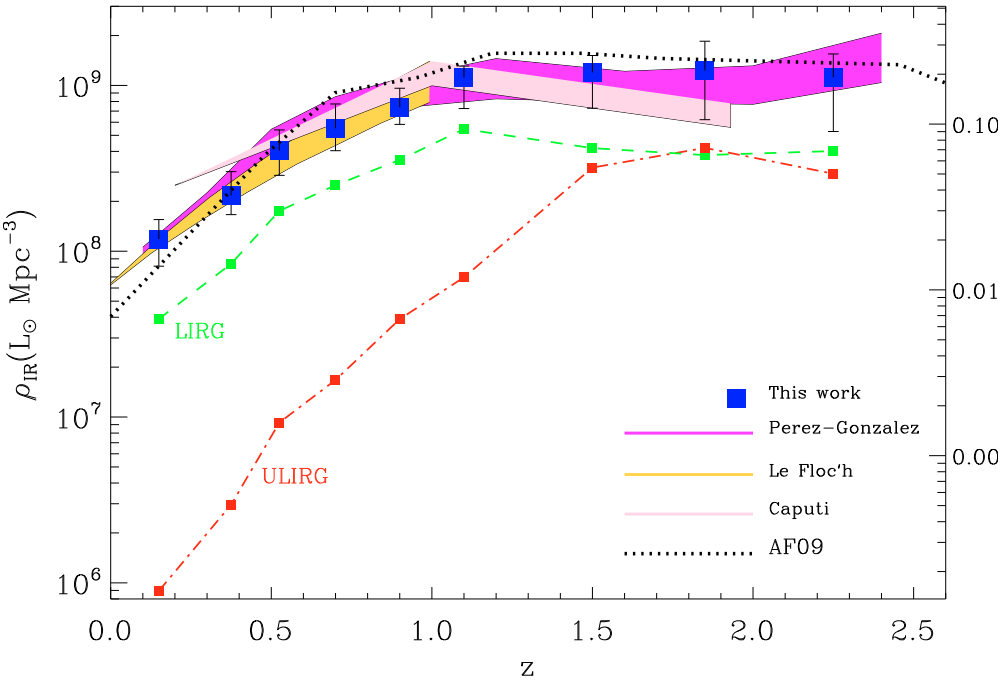

Fig. 16. Evolution of the comoving bolometric IR luminosity density with redshift. The right-hand axis contains the conversion to star-formation rate based on a scaling law by Kennicutt et al. (1998). The results from this work are presented as blue filled squares. The orange filled region is the results of Le Floc'h et al. (2005) up to $z \sim 1$, the light pink area marks the data obtained by Caputi et al. (2007, the $z = 0.2$ point comes from the bolometric IR LF derived from the 8 μm LF by Huang et al. 2007) and the magenta curve those by Perez-Gonzalez et al. (2005). We also report the separate contributions from LIRGs (here defined ad $10^{11}\ L_\odot < L_{IR} < 10^{12}\ L_\odot$, green dashed line) and ULIRGs ($L_{IR} > 10^{12}\ L_\odot$, red dot-dashed line) to the IR luminosity density. The black dotted line corresponds to the prediction from the model of Franceschini et al. (2009). In the redshift interval $0 < z < 1$, the bolometric IR luminosity density evolves as $(1 + z)^{3.8\pm0.4}$.

sources, they provide a tentative detection of a *downsizing* effect in the evolution of the IR galaxy populations, hence in the cosmic star formation history. This behaviour appears to be similar to one reported for a completely different population of cosmic sources, i.e., type-1 AGNs selected in X-rays and analyzed by Hasinger et al. (2005; see also Smolcic et al. 2009 for radio selected galaxies).

If confirmed, our results are obviously far more significant and far reaching, because they concern the bulk of the emission by the whole cosmic source population selected in the IR. In any case, this similarity between the evolutionary properties of our IR-selected galaxy population and those of X-ray AGNs strongly supports the case for co-eval AGN/starburst activity and a physical relation between the two populations.

7.4. Comparison with model predictions

We report in Figs. 4, 5, 9–12 and 16 a comparison of our results with predictions of a phenomenological model by Franceschini et al. (2009, AF09). The latter, in particular, are compared with the rest-frame 24 μm LF in Fig. 12 (dashed lines), showing generally good agreement. The low-z behaviour of the AF09 model has been calibrated on a variety of number count data at bright fluxes (including the IRAS all-sky IR counts and those from the *Spitzer* SWIRE project), which guarantees excellent control of the low-redshift universal emissivity in the IR.

Compared to previous analyses based on pre-*Spitzer* surveys (e.g., Franceschini et al. 2001), an important addition in AF09 was the introduction of an evolutionary component of very luminous IR galaxies dominating the cosmic IR emissivity at $z \sim 2$, and essentially absent or very rare locally, hence corresponding to extremely rapid evolution with cosmic time. This population uncovered by the analyzing the galaxy samples selected by the *Spitzer*/MIPS deep 24 μm and SCUBA sub-millimetre observations, while it was undetected by ISO.

In Fig. 16, we compare the redshift evolution of our derived cosmic star-formation rate with the AF09 model. The general trend is nicely reproduced, implying (with all the other observational constraints considered by the model) that the main features of the IR galaxy evolution are understood. Our results support a scenario where the fast evolution observed from $z = 0$ to 1 flattens above $z \sim 1$ and keeps approximately flat to $z \sim 2.5$. Both models and the present data provide clear evidence of a population of very luminous galaxies becoming increasingly important at $z > 1$. The current interpretation identifies these objects with the progenitors of spheroidal galaxies. A more detailed discussion will be given in AF09.

8. Summary

We have exploited a combination of data from the GOODS and VVDS-SWIRE multi-wavelength surveys to determine mid-IR and bolometric luminosity functions (and thus to estimate the SFR density) over a wide ($0 < z < 2.5$) redshift interval.

The primary sample for this analysis was selected from flux-limited samples of MIPS/*Spitzer* 24 μm sources in the GOODS (North and South) and VVDS-SWIRE fields, at the flux limits of $S(24\ \mu m)$ >80 μJy and $S(24\ \mu m)$ >400 μJy, respectively.

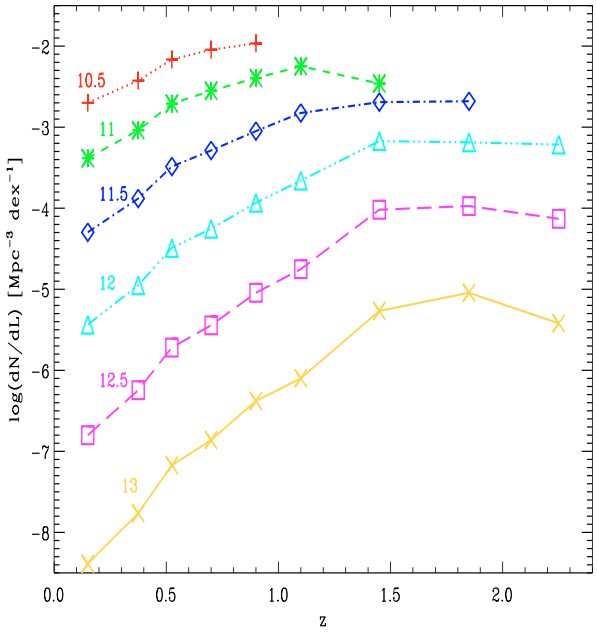

Fig. 17. The space density of IR selected galaxies as a function of redshift in different luminosity classes. The numbers with the same colour coding at the left side of each curve indicate the corresponding IR luminosity in solar units (logarithmic).

Our combined use of these two sensitivity thresholds helped us to obtain a wide coverage of the luminosity-redshift plane and ensure reliable statistics. We have performed a careful identification of the optical counterparts, by applying a maximum likelihood technique to the deeper GOODS surveys, while the identification was more straightforward at the brighter VVDS-SWIRE limits. We took advantage of the extensive spectroscopic information available in the GOODS fields and the high-quality photometric redshifts in the VVDS-SWIRE area, combined with the rich multiwavelength optical-to-IR datasets, to perform a fitting procedure on the entire SED for each source in our sample. In this way, we have been able to estimate the rest-frame luminosity at different wavelengths, and obtain the spectral extrapolations needed to compute the bolometric luminosity for each object.

We have computed rest-frame luminosity functions at 8, 12, 15, and 24 μm for comparison with a variety of previously published results at these wavelengths. We found a fairly good agreement with previous results at various rest-frame wavelengths and redshift bins.

We extrapolated total IR ([8−1000 μm]) luminosities from our best-fit to the SEDs of each source, and used these to derive the bolometric LF to $z \sim 2.5$. Adopting our fitting function, the number density of sources, as parameterized by Φ^*, evolves as e $(1+z)^{1.1}$ in the redshift range $0 < z < 1$, while the typical infrared luminosity (L^*) evolves as $(1+z)^{2.7}$. Above $z > 1$, the evolution degeneracy between number density and luminosity is more significant, but the comoving density is constrained to remain roughly constant with redshift. By integrating the best-fit LF in each redshift bin, we obtained a robust determination of the IR luminosity density to $z \sim 2$ and found general agreement with previously published results based on IR data. In the redshift range $0 < z < 1$, we find that the bolometric IR luminosity density evolves as $(1+z)^{3.8\pm0.4}$. At higher redshifts, our result seem to confirm a flattening of the IR luminosity density.

We estimated the separate contributions from LIRGs ($10^{11} < L_{\rm IR} < 10^{12}\,L_\odot$) and ULIRGs ($L_{\rm IR} > 10^{12}\,L_\odot$) to the IR luminosity density. At $z \sim 0.2$, ∼30% of the bolometric IR luminosity density originates in LIRGs and <1% in ULIRGs. At $z = 1$, the fractional contributions from LIRGs and ULIRGs are 45% and 6%, respectively. At $z \sim 2$, the contributions of LIRGs and ULIRGs become 48% and 45% of the total budget, respectively. This demonstrates that the cosmic evolution of the highest- and of the moderate-luminosity sources are therefore drastically different.

In comparison with model predictions by Franceschini et al. (2009, in preparation, but see also Franceschini et al. 2008), our results confirm a rapid increase in of the galaxy IR volume emissivity up to $z \sim 1$ and the evidence of a population of very luminous galaxies becoming dominant at $z > 1$.

Finally, our data seem to indicate a clear dependence on luminosity of the source comoving number density peak as a function of redshift: the brightest IR galaxies formed stars earlier in the cosmic history ($z >\sim 1.5$), while the star-formation activity of the less luminous begins later ($z \sim 1$ for $L_{\rm IR} < 10^{11}$). This confirms a *downsizing* pattern in the evolution of the IR emissivity of galaxy populations. This behaviour is at least qualitatively similar to what has already been detected for AGNs at other wavelengths, although our limited coverage of the faint end of the luminosity function prevents us from drawn more definite conclusions.

Acknowledgements. Part of this work was supported by the Italian Space Agency under contract ASI/INAF I/005/07/0 Herschel Fase E and under contract ASI/I/016/07/0. It is partly based on observations made with the *Spitzer* Space Telescope, which is operated by the Jet Propulsion Laboratory, California Institute of Technology under a contract with NASA.
This research has been developed within the framework of the VVDS consortium.
This work has been partially supported by the CNRS-INSU and its Programme National de Cosmologie (France), and by Italian Ministry (MIUR) grants COFIN2000 (MM02037133) and COFIN2003 (num.2003020150) and by INAF grants (PRIN-INAF 2005).
The VLT-VIMOS observations have been carried out on guaranteed time (GTO) allocated by the European Southern Observatory (ESO) to the VIRMOS consortium, under a contractual agreement between the Centre National de la Recherche Scientifique of France, heading a consortium of French and Italian institutes, and ESO, to design, manufacture and test the VIMOS instrument. Based on observations collected at the European Southern Observatory Very Large Telescope, Paranal, Chile, program 070.A-9007(A), and on data obtained at the Canada-France-Hawaii Telescope, operated by the Institut National des Sciences de l'Univers of the Centre National de la Recherche Scientifique of France, the National Research Council of Canada, and the University of Hawaii. Based on observations obtained with MegaPrime-MegaCam, a joint project of CFHT and CEA-DAPNIA, at the Canada-France-Hawaii Telescope (CFHT) which is operated by the National Research Council (NRC) of Canada, the Institut National des Science de l'Univers of the Centre National de la Recherche Scientifique (CNRS) of France, and the University of Hawaii. This work is based in part on data products produced at TERAPIX and the Canadian Astronomy Data Centre as part of the Canada-France-Hawaii Telescope Legacy Survey, a collaborative project of NRC and CNRS.
We warmly thank P. Perez-Gonzalez for useful discussion and for reading our work, Bob Mann for his advice and for his contribution to the ELAIS/IDL software which provided the basis for the likelihood & reliability analysis. We also thank F. Pozzi for providing her 15 μm luminosity function in electronic format and C. Gruppioni for useful comments.
We are finally grateful to the referee for his/her comments and suggestions that improved the presentation of the paper.

References

Alonso-Herrero, A., Pérez-González, P. G., Alexander, D. M., et al. 2006, ApJ, 640, 167
Arnouts, S., Walcher, C. J., Le Fèvre, O., et al. 2007, A&A, 476, 137
Babbedge, T. S. R., Rowan-Robinson, M., Vaccari, M., et al. 2006, MNRAS, 370, 1159
Ballantyne, D. R., & Papovich, C. 2007, ApJ, 660, 988

Barger, A. J., Cowie, L. L., & Wang, W.-H. 2008, ApJ, 689, 687
Bavouzet, N., Dole, H., Le Floc'h, E., et al. 2008, A&A, 479, 83
Bertin, E., & Arnouts, S. 1996, A&AS, 117, 393
Bolzonella, M., Miralles, J.-M., & Pelló, R. 2000, A&A, 363, 476
Capak, P., Cowie, L. L., Hu, E. M., et al. 2004, AJ, 127, 180
Caputi, K. I., Lagache, G., Yan, Lin, et al. 2007, ApJ, 660, 97
Chapman, S. C., Blain, A. W., Smail, I., & Ivison, R. J. 2005, ApJ, 622, 772
Chary, R., & Elbaz, D. 2001, ApJ, 556, 562
Chary, R., Casertano, S., Dickinson, M. E., et al. 2004, ApJS, 154, 80
Cowie, L. L., Barger, A. J., Hu, E. M., Capak, P., & Songaila, A. 2004, AJ, 127, 3137
de la Torre, S., Le Fèvre, O., Arnouts, S., et al. 2007, A&A, 475, 443
Desai, V., Soifer, B. T., Dey, A., et al. 2008, ApJ, 679, 1204
Dole, H., Rieke, G. H., Lagache, G., et al. 2004, ApJS, 154, 9
Elbaz, D., Cesarsky, C. J., Fadda, D., et al. 1999, A&A, 351, L37
Elbaz, D., Cesarsky, C. J., Chanial, P., et al. 2002, A&A, 384, 848
Fadda, D., Marleau, F. R., Storrie-Lombardi, L. J., et al. 2006, AJ, 131, 2859
Fang, F., Shupe, D. L., Xu, C., & Hacking, P. B. 1998, ApJ, 500, 693
Fiore, F., Grazian, A., Santini, P., et al. 2008, ApJ, 672, 94F
Franceschini, A., Danese, L., de Zotti, G., & Xu, C. 1988, MNRAS, 233, 175
Franceschini, A., Aussel, H., Cesarsky, C. J., Elbaz, D., & Fadda, D. 2001, A&A, 378, 1
Franceschini, A., Manners, J., Polletta, M., et al. 2005, AJ, 129, 2074
Franceschini, A., Rodighiero, G., Cassata, P., et al. 2006, A&A, 453, 397
Franceschini, A., Rodighiero, G., & Vaccari, M. 2008, A&A, 487, 837
Franceschini, A., Rodighiero, G., Vaccari, M., Marchetti, L., & Mainetti, G. 2009, A&A, accepted [arXiv:0906.4264]
Giavalisco, M., Ferguson, H. C., Koekemoer, A. M., et al. 2004, ApJ, 600, L93
Grazian, A., Fontana, A., de Santis, C., et al. 2006, A&A, 449, 951
Gruppioni, C., Pozzi, F., Polletta, M., et al. 2008, ApJ, 684, 136
Hacking, P., Houck, J. R., & Condon, J. J. 1987, ApJ, 316, L15
Hasinger, G., Miyaji, T., & Schmidt, M. 2005, A&A, 441, 417
Huang, J.-S., Ashby, M. L. N., Barmby, P., et al. 2007, ApJ, 664, 840
Huynh, M. T., Frayer, D. T., Mobasher, B., et al. 2007, ApJ, 667, L9
Kennicutt, R. C., Jr. 1983, ApJ, 272, 54
Kennicutt, R. C., Jr. 1998, ApJ, 498, 541
Ilbert, O., Tresse, L., Arnouts, S., et al. 2004, MNRAS, 351, 541
Ilbert, O., Arnouts, S., McCracken, H. J., et al. 2006, A&A, 457, 841
Iovino, A., McCracken, H. J., Garilli, B., et al. 2005, A&A, 442, 423
Lagache, G., Dole, H., Puget, J.-L., et al. 2004, ApJS, 154, 112
Lawrence, A., Warren, S. J., Almaini, O., et al. 2007, MNRAS, 379, 1599
Le Fèvre, O., Vettolani, G., Paltani, S., et al. 2004a, A&A, 428, 1043
Le Fèvre, O., Mellier, Y., McCracken, H. J., et al. 2004b, A&A, 417, 839
Le Fèvre, O., Vettolani, G., Garilli, B., et al. 2005, A&A, 439, 845
Le Floc'h, E., Papovich, C., Dole, H., et al. 2005, ApJ, 632, 169
Le Floc'h, E., Aussel, H., Ilbert, O., et al. 2009, ApJ, 703, 222
Lonsdale, C. J., Smith, H. E., Rowan-Robinson, M., et al. 2003, PASP, 115, 897
Magnelli, B., Elbaz, D., Chary, R. R., et al. 2009, A&A, 496, 57
Mancini, C., Matute, I., Cimatti, A., et al. 2009, A&A, 500, 705
Marleau, F. R., Fadda, D., Storrie-Lombardi, L. J., et al. 2004, ApJS, 154, 66
Marleau, F. R., Fadda, D., Appleton, P. N., et al. 2007, ApJ, 663, 218
McCracken, H. J., Radovich, M., Bertin, E., et al. 2003, A&A, 410, 17
Papovich, C., Dole, H., Egami, E., et al. 2004, ApJS, 154, 70
Pearson, C. P. 2001, MNRAS, 325, 1511
Pearson, C. 2005, MNRAS, 358, 1417
Pérez-González, P. G., Rieke, G. H., Egami, E., et al. 2005, ApJ, 630, 82
Polletta, M., Tajer, M., Maraschi, L., et al. 2007, ApJ, 663, 81
Popesso, P., Dickinson, M., Nonino, M., et al. 2009, A&A, 494, 443
Pozzi, F., Gruppioni, C., Oliver, S., et al. 2004, ApJ, 609, 122
Puget, J. L., Lagache, G., Clements, D. L., et al. 1999, A&A, 345, 29
Ravikumar, C. D., uech, M., Flores, H., et al. 2007, A&A, 465, 1099
Radovich, M., Arnaboldi, M., Ripepi, V., et al. 2004, A&A, 417, 51
Rodighiero, G., Lari, C., Pozzi, F., et al. 2006, MNRAS, 371, 1891
Rowan-Robinson, M., Mann, R. G., Oliver, S. J., et al. 1997, MNRAS, 289, 490
Rush, B., Malkan, M. A., & Spinoglio, L. 1993, ApJS, 89, 1
Sanders, D. B., Mazzarella, J. M., Kim, D.-C., Surace, J. A., & Soifer, B. T. 2003, AJ, 126, 1607
Santini, P., Fontana, A., Grazian, A., et al. 2009, A&A, 504, 751
Sajina, A., Yan, L., Armus, L., et al. 2007, ApJ, 664, 713S
Sajina, A., Yan, L., & Lutz, D. 2008, ApJ, 683, 659S
Saunders, W., Rowan-Robinson, M., Lawrence, A., et al. 1990, MNRAS, 242, 318
Schmidt, M. 1968, ApJ, 151, 393
Shupe, D. L., Fang, F., Hacking, P. B., & Huchra, J. P. 1998, ApJ, 501, 597
Shupe, D. L., Rowan-Robinson, M., Lonsdale, C. J., et al. 2008, AJ, 135, 1050
Smolcic, V., Zamorani, G., Schinnerer, E., et al. 2009, ApJ, 696, 24
Soifer, B. T., Helou, G., & Werner, M. 2008, ARA&A, 46, 201
Surace, J., et al. 2005, The SWIRE Data Release 2, SSC
Sutherland, W., & Saunders, W. 1992, MNRAS, 259, 413
Takeuchi, T. T., Buat, V., Iglesias-Páramo, J., Boselli, A., & Burgarella, D. 2005, A&A, 432, 423
Vaccari, M., Marchetti, L., Franceschini, A., & Perez-Fournon, I. 2009 [arXiv:0902.0248]
Vanzella, E., Cristiani, S., Dickinson, M., et al. 2005, A&A, 434, 53
Vanzella, E., Cristiani, S., Dickinson, M., et al. 2006, A&A, 454, 423
Vanzella, E., Cristiani, S., Dickinson, M., et al. 2008, A&A, 478, 83
Tresse, L., Ilbert, O., Zucca, E., et al. 2007, A&A, 472, 403
Warren, S. J., Hambly, N. C., Dye, S., et al. 2007, MNRAS, 375, 213
Werner, M. W., Roellig, T. L., Low, F. J., et al. 2004, ApJS, 154, 1
Wolf, C., Meisenheimer, K., Kleinheinrich, M., et al. 2004, A&A, 421, 913
Wuyts, S., Labbe, I., Forster Schreiber, N. M., et al. 2008, ApJ, 689, 653
Yan, Lin, Sajina, A., Fadda, D., et al. 2007, ApJ, 658, 778
Xu, C., Lonsdale, C. J., Shupe, D. L., O'Linger, J., & Masci, F. 2001, ApJ, 562, 179
Xu, C. K., Lonsdale, C. J., Shupe, D. L., et al. 2003, ApJ, 587, 90
Zheng, X. Z., Bell, E. F., Rix, H.-W., et al. 2006, ApJ, 640, 784